Eur. Phys. J. C (2025) 85:1352
https://doi.org/10.1140/epjc/s10052-025-15072-2

THE EUROPEAN PHYSICAL JOURNAL C

Regular Article - Theoretical Physics

Global monopole induced wormholes in power-law gravity: stability and physical viability

M. Yousaf[1,2,a], **H. Asad**[3,b], **Kashif Ammar Yasir**[4,c], **S. K. Maurya**[5,d], **Akram Ali**[6,e], **Farruh Atamurotov**[7,8,9,f]

[1] Department of Mathematics, Virtual University of Pakistan, 54-Lawrence Road, Lahore 54000, Pakistan
[2] Research Center of Astrophysics and Cosmology, Khazar University, 41 Mehseti Street, AZ1096 Baku, Azerbaijan
[3] Institute of Energy and Environmental Engineering, University of the Punjab, Quaid-i-Azam Campus, Lahore 54590, Pakistan
[4] Department of Physics, Zhejiang Normal University, Jinhua 321004, China
[5] Department of Mathematical and Physical Sciences, College of Arts and Sciences, University of Nizwa, Nizwa 616, Sultanate of Oman
[6] Department of Mathematics, College of Sciences, King Khalid University, Abha 61413, Saudi Arabia
[7] Kimyo International University in Tashkent, Shota Rustaveli str. 156, Tashkent 100121, Uzbekistan
[8] University of Tashkent for Applied Sciences, Str. Gavhar 1, Tashkent 100149, Uzbekistan
[9] Tashkent State Technical University, Tashkent 100095, Uzbekistan

Received: 23 September 2025 / Accepted: 13 November 2025

Abstract In this manuscript, we examine geometrical and physical properties of wormhole ($\mathcal{WH}$) solutions with monopole charge by considering three distinct shape function models in power-law gravity, i.e., Starobinsky $f(R)$ gravity, where R is Ricci scalr. The modified gravitational field equations are solved under the assumption of anisotropic energy–momentum tensor ($\mathcal{EMT}$), with particular attention given to the role of exotic matter ($\mathcal{EM}$) in sustaining these solutions. The impact of the global monopole charge ($\mathcal{GMC}$) is examined in detail, revealing that higher monopole charges enlarge the throat radius and produce flatter embedding surfaces through two and three dimensional embedding diagrams, thereby affecting both traversability and structural stability. A comprehensive investigation of physical quantities, energy conditions and stability analysis is carried out using several physical and geometrical criteria, including the adiabatic index approach, Herrera's cracking criterion, and causality conditions approach, along with anisotropic effects. Moreover, the total amount of $\mathcal{EM}$ is quantified through the volume integral quantifier method. These findings highlight supportive directions for future explorations of exotic spacetime structures in both theoretical and astrophysical contexts.

[a] e-mails: myousaf.math@gmail.com; m.yousaf@vu.edu.pk
[b] e-mails: hamnaasad2596@gmail.com; hamna.ieee@pu.edu.pk
[c] e-mail: kashif_ammar@yahoo.com (corresponding author)
[d] e-mail: sunil@unizwa.edu.om (corresponding author)
[e] e-mail: akali@kku.edu.sa
[f] e-mail: atamurotov@yahoo.com

1 Introduction

Observational cosmology over the past few decades reached on the remarkable conclusion that the cosmos is currently experiencing an accelerated expansion phase, while this unexpected phenomenon challenges the explanatory power of general theory of relativity ($\mathcal{GTR}$) when applied with conventional matter energy components [1–5]. To address this deficiency, a variety of theoretical frameworks proposed, which either introduce novel exotic fluids, commonly termed dark energy ($\mathcal{DE}$), or modify the underlying gravitational theory itself [6–8]. These modified approaches aim to resolve challenges such as the nature of dark matter ($\mathcal{DM}$), the origin of $\mathcal{DE}$, and the evolution of large scale cosmic formations [9–15].

Among alternative gravity theory $\mathcal{AGT}$ approaches, $f(R)$ gravity stands out due to its relative mathematical simplicity and rich phenomenology, these theories incorporate higher order curvature corrections capable of explaining cosmic acceleration without explicit $\mathcal{DE}$. However, the reformulated field equations in $f(R)$ gravity become significantly more complex, incorporating higher order derivatives that offer significant ground for testing deviations from $\mathcal{GTR}$ in astrophysical scenarios. Several important models of $f(R)$ gravity proposed to address a variety of cosmological issues like: Buchdahl model introduced by Hans Adolph Buchdahl in 1970, this model features a logarithmic modification of gravity, initially utilizing ψ instead of generic function's notation f as the arbitrary function [16] which is designed to explain

Published online: 25 November 2025

both the accelerated expansion of the universe at early and late times, this model gained significant attention following Starobinsky's work in 1980. The Starobinsky model introduced a quadratic term to the Ricci scalar R, playing a crucial role in explaining cosmic inflation [17], which laid the foundation for the field of inflationary cosmology and influenced subsequent developments in $\mathcal{AGT}$. Nojiri–Odintsov model incorporated both positive and negative powers of R, offering a unified framework to explain both the inflationary epoch in the early universe and the accelerated expansion at late times [18,19], while the Hu-Sawicki model designed to account for the effects of $\mathcal{DE}$ while respecting local gravity constraints, which is one of the most viable $f(R)$ models to simultaneously explain cosmic acceleration and pass solar system tests [20,21].

The Starobinsky model, defined by $f(R) = R + \beta R^2$, which is one of the earliest and most celebrated $f(R)$ theories, underpins successful inflationary scenarios and conforms well to observable data [17]. Extensive investigations continue to explore the theoretical consistency and observational viability of these models across various astrophysical and cosmological regimes [22–25]. Beyond cosmology, the impact of $f(R)$ and other $\mathcal{AGT}$s extends profoundly to compact objects, while the modifications influence horizon structure, thermodynamic traits, and quasi normal mode spectra. It also increasing our understanding of strong gravity phenomena [26], particularly, $f(R)$ gravity predicts an additional scalar polarization mode in gravitational wave signals beyond the two intrinsic transverse tensor modes of $\mathcal{GTR}$ [27,28].

The $\mathcal{WH}$s, solutions describing bridges between two separate regions of spacetime, have long captivated the theoretical physics community as exotic constructs permitted in $\mathcal{GTR}$. The theoretical roots of $\mathcal{WH}$ physics date back to 1916, when Ludwig Flamm identified a significant solution to Einstein's field equations that suggested a tunnel-like connection through spacetime [29]. This concept gained further clarity in 1935 when Einstein and Rosen proposed the Einstein–Rosen bridge, as a singularity free model of elementary particles [30]. However, Fuller and Wheeler demonstrated that such $\mathcal{WH}$s are inherently unstable, incapable of supporting traversable pathways for light or matter [31].

The study of $\mathcal{WH}$s took a significant turn with the emergence of the Ellis–Bronnikov model, independently developed by Ellis [32] and Bronnikov [33]. Interest in traversable $\mathcal{WH}$s reignited during the 1980*s* through the pioneering efforts of Morris and Thorne, who formalized the conditions under which a $\mathcal{WH}$ could be safely traversed by matter without encountering horizons [34]. Central to their framework was the requirement for $\mathcal{EM}$, i.e., (a hypothetical material characterized by a negative energy density that could counteract gravitational collapse). This concept extended by Wang et al., who introduced dynamic time dependent $\mathcal{WH}$ geometries [35], however, a recurring challenge across such models is the violation of classical energy conditions, especially the null energy constrains ($\mathcal{NEC}s$), weak energy constrains ($\mathcal{WEC}s$), strong energy constrains ($\mathcal{SEC}s$) and dominant energy constrains ($\mathcal{DEC}s$), which are usually considered essential for physically meaningful energy momentum distributions [36–39].

In conventional $\mathcal{GTR}$ the $\mathcal{WH}$s require $\mathcal{EM}$ content that violates the $\mathcal{NEC}$ to remain traversable and stable [34,36]. The $\mathcal{AGT}$s, however, shift this paradigm by attributing the $\mathcal{NEC}$ violations to effective geometrical terms or higher curvature corrections rather than physically exotic fields and this conceptual advance opens the door to the construction of $\mathcal{WH}$ geometries potentially sustained by physically reasonable matter in $f(R)$ theory and scalar tensor theories [15,40–43]. Another interesting direction involves solutions with the vanishing Ricci scalar R, yielding globally regular, traversable $\mathcal{WH}$s with arbitrary throat sizes and both symmetric and asymmetric profiles which satisfy vacuum field equations on the brane, a hypersurface embedded in higher dimensional space as envisioned in string theory, and receive their effective stress energy from bulk gravitational interactions [44]. Further exploration by Furey et al. [45] introduced higher-order curvature corrections into the gravitational action, including nonlinear functions of the Ricci scalar. Their work demonstrated that violations of the $\mathcal{WEC}$ could be localized and minimized at the $\mathcal{WH}$ throat, allowing static configurations that remain traversable without requiring global exoticity. This throat-focused approach offered a novel perspective on the feasibility of $\mathcal{WH}$ solutions in $\mathcal{AGT}$ contexts.

Some studies performed to explored the possibility of galactic $\mathcal{WH}$s, where the $\mathcal{WH}$ geometries considered to be embedded in a galactic halo dominated by $\mathcal{DM}$ or exotic fields. The stability and observational signatures of these entities may differ from isolated $\mathcal{WH}$s which exhibit intriguing astrophysical implications, such as gravitational lensing effects, stable halo supported structures, and potential observational signatures within galactic scale systems [46,47]. The traversable $\mathcal{WH}$s sourced by $\mathcal{DM}$ in loop quantum cosmology studied in [48] and the exploration of galactic $\mathcal{WH}$s not only bridges the gap between astrophysical observations and $\mathcal{AGT}$s but also provides new insights into the role of $\mathcal{DE}$ and topological defects in the galactic structure. Such studies are complementary to the ordinary $\mathcal{WH}$ models and suggest potential pathways for connecting local geometric deformations with galactic-scale dynamics [49–53]. Whereas the present work is primarily devoted to the construction and stability analysis of static $\mathcal{WH}$ geometries, the idea of galactic $\mathcal{WH}$s provides an astrophysically motivated frame that complements our results and suggests possible extensions of the current model to more realistic cosmic scenarios. Some relevant studies that addressed possible stable behavior, via-

bility, and physical aspects of compact structures, charged configurations, and $\mathcal{WH}$ geometries in $\mathcal{AGT}$ models with and without charged anisotropic effects on different compact structures [43,54–66].

Numerous studies expanded this theme, analyzing $\mathcal{WH}$s in diverse theoretical settings such as non-commutative geometries [67], $f(R)$ gravity [68], and some extra scalar field scenarios [69–71]. Furthermore, dynamical $\mathcal{WH}$ configurations evolving towards cosmological backgrounds attracted attention [72], whereas a concurrent focus placed on quasi-normal modes, perturbative signatures that encode stability properties and offer the potential for experimental distinguishability between $\mathcal{WH}$s and black holes via gravitational wave echoes or ringdown signals [73]. Building upon these developments, the existing literature investigates traversable $\mathcal{WH}$s in the Starobinsky $f(R)$ model augmented by a cloud of strings, a topological defect that mimics a relic cosmological structure, although $\mathcal{WH}$ solutions sourced from string clouds studied in [74]. The incorporation of this ingredient within $f(R)$ gravity remains largely unexplored.

The $\mathcal{WH}$ physics came into the spotlight with several $\mathcal{AGT}$s to overcome the limitations of $\mathcal{GTR}$, particularly its reliance on $\mathcal{EM}$ to sustain traversable $\mathcal{WH}$s. In the context of conformal Weyl gravity built on conformally invariant actions, while Lobo et al. [75] revealed that this theory allows $\mathcal{WH}$ solutions to be solved without classical energy condition violations due to the presence of an effective $\mathcal{EMT}$, highlighting the capacity of higher order curvature terms to influence the spacetime structure in novel ways. Expanding further, the $f(R,T)$ $\mathcal{AGT}$ in which both the Ricci scalar R and the trace of the $\mathcal{EMT}$ T appear in the action showed that matter obeying classical energy conditions can still support $\mathcal{WH}$ geometries. Here, it is the effective geometric contributions, rather than the physical matter, that explain the violation of the $\mathcal{NEC}$. The higher order curvature effects in such models can provide the necessary conditions for $\mathcal{WH}$ existence without exotic inputs [76–79]. Comparative analyzes among $f(R)$, $f(R,T)$, and other $\mathcal{GTR}$ frameworks continue to shed light on the unique characteristics of these $\mathcal{AGT}$s [80].

Yousaf et al. [81] studied the construction of $\mathcal{WH}$s through diverse $\mathcal{DM}$ density profiles, while in the framework of extended teleparallel gravity with matter coupling, traversable $\mathcal{WH}$ solutions were examined in [50], whereas phantom traversable $\mathcal{WH}$s in modified teleparallel gravity were presented in [82]. Moreover, traversable $\mathcal{WH}$s in $\mathcal{AGT}$, focusing on geometry, energy conditions, and gravitational lensing, were analyzed in [53]. New relativistic traversable $\mathcal{WH}$ solutions and energy constraints within the Rastall teleparallel gravitational paradigm were investigated in [83], additionally, Ditta et al. [84] provided novel insights into $\mathcal{WH}$ solutions, while astrophysical signatures of traversable $\mathcal{WH}$s in $\mathcal{AGT}$, considering different equations of state and different dynamical analysis, were discussed in [85–90].

In many of these theories, the field equations resemble Einstein's equations but include two distinct contributions: one from ordinary matter and the other from modifications to the gravitational sector, this type of fluid interpretation encourages the exploration of whether ordinary matter, in the presence of geometric modifications, might support stable $\mathcal{WH}$ structures under appropriate constraints. In this work, we considered the Starobinsky model which also known as power law gravity model. In contrast, the inclusion of different toy models of shape functions of $\mathcal{WH}$s introduces novel geometric features, making this frame an ideal tool for exploring the richness of $\mathcal{AGT}$ $\mathcal{WH}$ phenomenology.

By getting motivation from these developments we investigate some astrophysical properties of $\mathcal{WH}$ geometries under the influence monopole charge by considering some specific $\mathcal{WH}$ shape function models with the impact of Starobinsky $f(R)$ gravity model, i.e., $f(R) = R + \beta R^2$, where R is Ricci scalr and β a correction parameter to $\mathcal{AGT}$. We conceived modified gravitational field equations under this assumption with anisotropic $\mathcal{EMT}$. The impact of $\mathcal{GMC}$ is examined in detail, revealing that higher monopole charges enlarge the throat radius and produce flatter embedding surfaces through two and three dimensional embedding diagrams and also a comprehensive investigation of physical quantities, energy conditions and stability analysis is carried out using several physical and geometrical criteria, including the adiabatic index approach, Herrera's cracking criterion, and causality conditions approach, along with anisotropic effects in $f(R)$ gravity model and effects of the $\mathcal{GMC}$. To measure the $\mathcal{EM}$ content we used the volume integral quantifier (VIQ) which is needed necessary to sustain the $\mathcal{WH}$'s traversablity.

The paper is organized as: first section covers introductory information of the topic and literature review, while in second section, we present basic formalism of Morris–Thorne type $\mathcal{WH}$ and considered model of $f(R)$ gravity. In third section, we discuss three $\mathcal{WH}$ shape function models and embedding diagrams. In fourth section, we evaluate $\mathcal{WH}$ models and graphical analysis along with an explanation of the physical quantities. fifth section presents the stability analysis with different tests and the measurement of unusual matter content using VIQ technique. The last section concludes by summarizing the findings and discussing their broader implications for $\mathcal{WH}$ physics in extended gravity scenarios.

2 Basic formalism of Morris–Thorne type $\mathcal{WH}$ and Starobinsky model

To continue our systematic investigation, a static, spherically symmetric Morris–Thorne type $\mathcal{WH}$ time independent met-

ric [91,92] in Schwarzschild coordinates (t, r, θ, ψ), is considered in the following form:

$$ds^2 = g_{\xi\zeta}dx^{\xi}dx^{\zeta} = diag\left\{-e^{2\Phi(r)},\ \alpha^{-2}\left(1-\frac{A(r)}{r}\right)^{-1},\ r^2,\ r^2\sin^2\theta\right\}, \tag{1}$$

here in this line element $\Phi(r)$ is the redshift function, and $A(r)$ representing the shape function that governs the spatial configuration of the $\mathcal{WH}$. This metric is especially useful in modeling hypothetical objects like $\mathcal{WH}$s, which are theorized to be passageways connecting distinct regions of spacetime [93,93–96] and α is linked to the monopole defect and is expressed as

$$\alpha \approx 1 - 8\pi\varpi^2, \tag{2}$$

here ϖ a symmetry-breaking scale [97–99] and presence of a monopole introduces a solid angle deficit approximately given by

$$\delta\Omega \approx 2\pi(1-\alpha). \tag{3}$$

To ensure physical consistency:

$$0 \leq 8\pi\varpi^2 < 1 \quad \Rightarrow \quad 0 < \alpha \leq 1, \tag{4}$$

which restricts the $\mathcal{GMC}$ to the admissible range $0 < \alpha \leq 1$ [91]. In this metric, each term provides specific information about the nature of spacetime the first term accounts for time dilation due to gravitational effects. We enforce the condition that $\Phi(r)$ is constant, thus eliminating the formation of event horizons, i.e., $\Phi'(r) = 0$, while the radial term describes the spatial stretching in the radial direction. The function $A(r)$, the shape function, defines the $\mathcal{WH}$'s geometry, and α^2 is a factor associated with topological effects like those induced by a $\mathcal{GMC}$. This is an additional parameter that accounts for symmetry breaking phenomena within spacetime, while last two terms reflect the standard angular geometry of a spherically symmetric spacetime. To preserve the $\mathcal{WH}$'s traversability, we require that no event horizon exists, which leads to assuming a constant redshift function, consequently the simplified form of above line element is give as [91,92]:

$$ds^2 = g_{\xi\zeta}dx^{\xi}dx^{\zeta} = diag\left\{-1,\ \alpha^{-2}\left(1-\frac{A(r)}{r}\right)^{-1},\ r^2,\ r^2\sin^2\theta\right\}, \tag{5}$$

Let us turn our attention to the matter content within the $\mathcal{WH}$, modeled by an anisotropic fluid described by the $\mathcal{EMT}$ as:

$$T^{(m)}_{\xi\zeta} = (\rho + p_t)U_{\xi}U_{\zeta} + (p_r - p_t)\eta_{\xi}\eta_{\zeta} + p_t g_{\xi\zeta}, \tag{6}$$

here ρ is the energy density, p_r is the radial pressure, and p_t is the tangential pressure. The four-velocity U_{ξ} and the unit radial vector η_{ξ} account for the fluid's motion and orientation.

In this work, we will utilize the metric formalism of $f(R)$ gravity framework, which generalizes the Einstein–Hilbert action by replacing the Ricci scalar R with a general function $f(R)$, which allows for richer gravitational dynamics, and its action is given by:

$$H_{f(R)} = \frac{1}{2\kappa}\int_{\Omega} d^4x\sqrt{-g}\,f(R) + \int L^{(m)}\sqrt{-g}\,d^4x, \tag{7}$$

where Ω denotes a four-dimensional spacetime manifold equipped with a metric $g_{\xi\zeta}$ also $\kappa = 8\pi G$, and g is the determinant of the metric tensor $g_{\xi\zeta}$. In this work, we consider the Starobinsky model [17,100,101], one of the simplest and most widely studied models of $f(R)$ gravity, defined by:

$$f(R) = R + \beta R^2, \tag{8}$$

where β is a constant parameter that controls the deviation from the standard $\mathcal{GTR}$. To continue our systematic investigation, we consider modified field equations of $f(R)$ gravity which are obtained by varying the action given in Eq. (7) with respect to the metric $g_{\xi\zeta}$ as:

$$f_R R_{\xi\zeta} - \frac{1}{2}f g_{\xi\zeta} + \left(g_{\xi\zeta}\Box - \nabla_{\xi}\nabla_{\zeta}\right)f_R = \kappa T_{\xi\zeta}, \tag{9}$$

where $f_R \equiv \frac{df}{dR} = 1 + 2\beta R$, $\Box = g^{\xi\zeta}\nabla_{\xi}\nabla_{\zeta}$ is the d'Alembertian operator, and $T_{\xi\zeta}$ is the standard $\mathcal{EMT}$ and the trace equation is given as:

$$3\Box f_R + f_R R - 2f = \kappa T, \tag{10}$$

where $T = T^{\xi}_{\xi}$ is the trace of the $\mathcal{EMT}$. The additional degrees of freedom introduced by term βR^2 allow for significant deviations from $\mathcal{GTR}$, especially in regimes of strong gravity, and this feature makes the Starobinsky model a compelling choice for investigating compact objects as well as exotic space-times, such as $\mathcal{WH}$s, in the context of $\mathcal{AGT}$s. The Ricci scalar, which is a trace of the curvature, is computed as: $R = 2/r^2(1 - \alpha^2 + \alpha^2 A'(r))$. This provides the foundation for solving the modified field equations in the context of $f(R)$ gravity, which are required to describe the behavior of the $\mathcal{WH}$ under different matter distributions and topological influences. We compute the non-zero components of the modified field equations (9) by using the s$\mathcal{EMT}$,

along with the substitution of the considered Starobinsky model. We arrive at the following simplified expression:

$$\rho = \frac{1}{r^5}\Big[2\alpha^2\beta A(r)\big(-6\alpha^2+2\alpha^2r^2A'''(r) - 5\alpha^2rA''(r)+6\alpha^2A'(r)+6\big) + r\Big(10\alpha^4\beta-12\alpha^2\beta-4\alpha^4\beta r^2A'''(r) + 8\alpha^4\beta rA''(r)-2\alpha^4\beta A'(r)^2+\alpha^2A'(r)\big(-8\alpha^2\beta + 2\alpha^2\beta rA''(r)+r^2\big)+2\beta-\alpha^2r^2+r^2\Big)\Big] \tag{11}$$

$$p_r = \frac{1}{r^5}\Big[r\Big(8\alpha^4\beta rA''(r)+2\alpha^4\beta A'(r)^2-16\alpha^4\beta A'(r) + \big(\alpha^2-1\big)\big(14\alpha^2\beta+2\beta+r^2\big)\Big)-\alpha^2A(r)\big(12\alpha^2\beta + 8\alpha^2\beta rA''(r)-12\alpha^2\beta A'(r)-12\beta+r^2\big)\Big] \tag{12}$$

$$p_t = \frac{1}{2r^5}\Big[\alpha^2A(r)\big(36\alpha^2\beta-8\alpha^2\beta r^2A'''(r)+28\alpha^2\beta rA''(r) - 36\alpha^2\beta A'(r)-36\beta+r^2\big)+r\Big(8\alpha^4\beta A'(r)^2 +4\beta\big(-7\alpha^4+6\alpha^2+2\alpha^4r^2A'''(r)-6\alpha^4rA''(r)+1\big) - \alpha^2A'(r)\big(-4\big(5\alpha^2+3\big)\beta+4\alpha^2\beta rA''(r)+r^2\big)\Big)\Big] \tag{13}$$

These are the expressions for the energy density, radial, and tangential pressure, respectively. We use these physical quantities and evaluate different energy conditions, stability, anisotropy parameters, and measure of total amount of $\mathcal{EM}$ in the following sections.

3 Wormhole shape function models

We construct traversable $\mathcal{WH}$ geometries by considering suitable choice of the shape function $A(r)$. It must satisfy several physical and geometrical constraints to ensure the viability and stability of the configuration. Specifically, the following conditions must hold:

- Throat condition: $A(a_0) = a_0$, where a_0 is the radius of the $\mathcal{WH}$ throat.
- Flaring-out condition: $A(r) - A'(r)r > 0$ at or near the throat.
- Radial constraint: $\frac{A(r)}{r} < 1$ for $r > a_0$.
- Asymptotic flatness: $\frac{A(r)}{r} \to 0$ as $r \to \infty$.
- Derivative constraint: $A'(a_0) < 1$ at the throat.

In this section, we explore analytically tractable shape function models that satisfy the above requirements in the presence of a $\mathcal{GMC}$ field, while these models help to visualize the geometry of the $\mathcal{WH}$, assess the energy conditions, and examine the anisotropic pressures. The three considered models of shape functions [91,100] given as:

$$A(r) = a_0\left[\tau_1\left(1-\frac{a_0}{r}\right)+1\right], \tag{14}$$

$$A(r) = r\,\exp\left[\tau_2(a_0-r)\right], \tag{15}$$

$$A(r) = a_0\tan^{-1}(\tau_3 r). \tag{16}$$

We present both 2D and 3D embedding diagrams which provide spatial visualizations of the $\mathcal{WH}$ throat. The 3D diagrams depict a surface of revolution by embedding a spatial slice (t = constant, $\theta = \pi/2$) into a Euclidean space, while to visualize the embedded diagrams of the $\mathcal{WH}$s represented by the toy shape functions (14), (15), and (16), we use an equatorial slice $\theta = \pi/2$ at a fixed time t = constant. This allows us to reduce the metric (5) into the following form:

$$\mathrm{d}s^2 = \frac{\mathrm{d}r^2}{\alpha^2\left(1-\frac{A(r)}{r}\right)} + r^2\mathrm{d}\psi^2. \tag{17}$$

In cylindrical coordinates, the Euclidean space metric is given by:

$$\mathrm{d}s^2 = \mathrm{d}z^2+\mathrm{d}r^2+r^2\mathrm{d}\psi^2. \tag{18}$$

Since the embedded surface in three-dimensional Euclidean space is expressed by $z = z(r)$, Eq. (18) can be rewritten as:

$$\mathrm{d}s^2 = \left[1+\left(\frac{\mathrm{d}z}{\mathrm{d}r}\right)^2\right]\mathrm{d}r^2+r^2\mathrm{d}\psi^2 \tag{19}$$

Comparing the recast metric (19) with the reduced metric (17), we get:

$$\frac{\mathrm{d}z}{\mathrm{d}r} = \pm\sqrt{\frac{1}{\alpha^2\left(1-\frac{A(r)}{r}\right)}-1}, \tag{20}$$

The obtained relation represents the embedded surface of the $\mathcal{WH}$. According to the flaring out condition, the inverse embedding function $r(z)$ satisfies $\frac{\mathrm{d}^2r}{\mathrm{d}z^2} > 0$ near the throat and also from Eq. (20), it follows that $\frac{\mathrm{d}z}{\mathrm{d}r} \to \infty$ at the throat, while the geometry becomes asymptotically flat as $r \to \infty$. The embedding profiles corresponding to the shape functions (14), (15), and (16) are illustrated in Figs. 1, 2, and 3, respectively.

These diagrams confirm the flaring-out condition at the throat ($r = a_0$), where the embedded surface becomes ver-

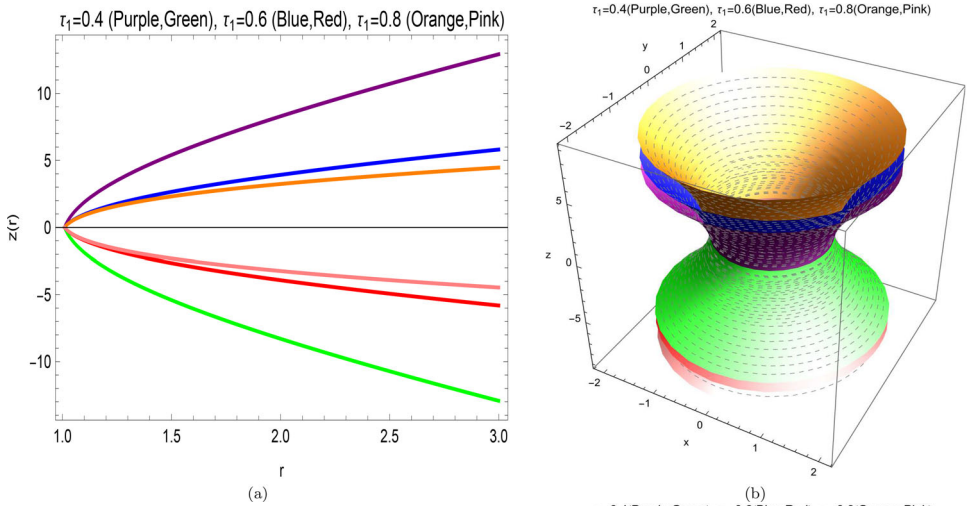

Fig. 1 2D panel (**a**) and 3D panel (**b**) embedding diagrams for $\mathcal{WH}$ defined by shape function (14) at $a_0 = 1$ with various parameter values

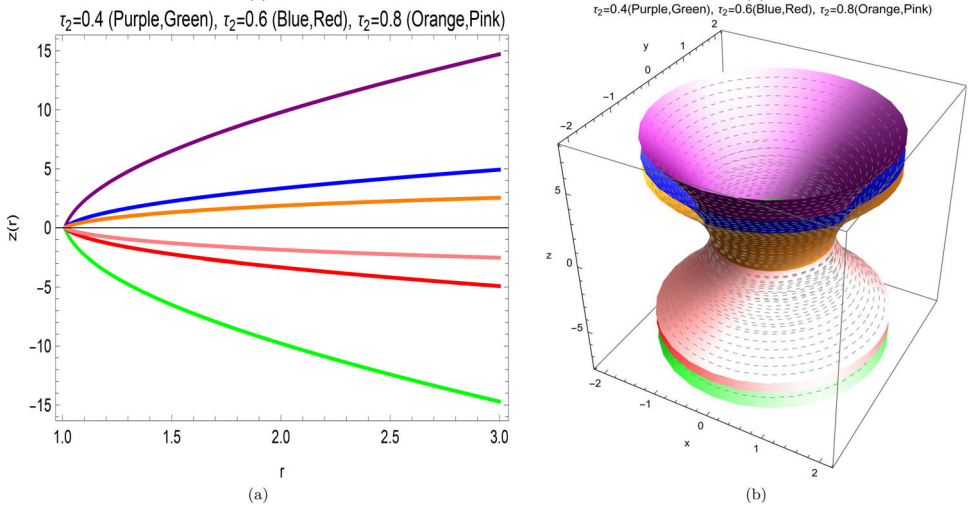

Fig. 2 2D panel (**a**) and 3D panel (**b**) embedding diagrams for $\mathcal{WH}$ defined by shape function (15) at $a_0 = 1$ with various parameter values

tical, i.e., $\frac{dz}{dr} \to \infty$. As $r \to \infty$, the surface flattens, indicating asymptotic flatness, i.e., $\frac{dz}{dr} \to 0$. The embedded diagrams also illustrate the effect of the model parameters on the $\mathcal{WH}$ geometry. For the shape function (14), increasing τ_1 reduces the height of the $\mathcal{WH}$. For (15), increasing τ_2 has a similar geometric impact. The shape function (16), with constants a_0 and τ_3, has an advantage over polynomial functions because $A(r)/r \to 0$ more rapidly. The diagrams (see Fig. 3) confirm that this shape function satisfies all $\mathcal{WH}$ criteria [102]. In both cases, increasing the model parameters gradually increases the height of the $\mathcal{WH}$. The embedding diagrams show the $\mathcal{WH}$'s upper and lower surfaces, linking two asymptotically flat regions through a throat at $r = a_0$, with symmetry about $z = 0$. Mesh grids on the 2D diagrams emphasize curvature, and colored curves mark the two solution branches. The embedding function $z(r)$ has a minimum at the throat, while the $\mathcal{GMC}$ α affects both throat width and curvature: larger α produces wider, flatter throats, enhancing stability and traversability.

4 Wormhole shape function models and graphical analysis

In $\mathcal{GTR}$ and $\mathcal{AGT}$s , energy conditions namely $\mathcal{NEC}$, $\mathcal{WEC}$, $\mathcal{SEC}$ and $\mathcal{DEC}$ are used to constrain the $\mathcal{EMT}$ and ensure physically reasonable matter distributions, for an anisotropic fluid with energy density ρ, radial pressure p_r, and tangential pressure p_t, the conditions are mathematically represented as follows:

- $\mathcal{NEC}$: $\rho + p_i \geq 0$ $(i = r,\ t)$ which implies that for any null vector k^ξ, the energy density measured by a light-like observer is non-negative: $T_{\xi\zeta}k^\xi k^\zeta \geq 0$. It is the weakest of all energy conditions and is crucial in the Raychaudhuri equation to prevent the formation of singularities or ensure geodesic convergence, while violation of the $\mathcal{NEC}$ typically signals the presence of $\mathcal{EM}$, which is $\mathcal{NEC}$essary for maintaining traversable $\mathcal{WH}$s and warp drives.

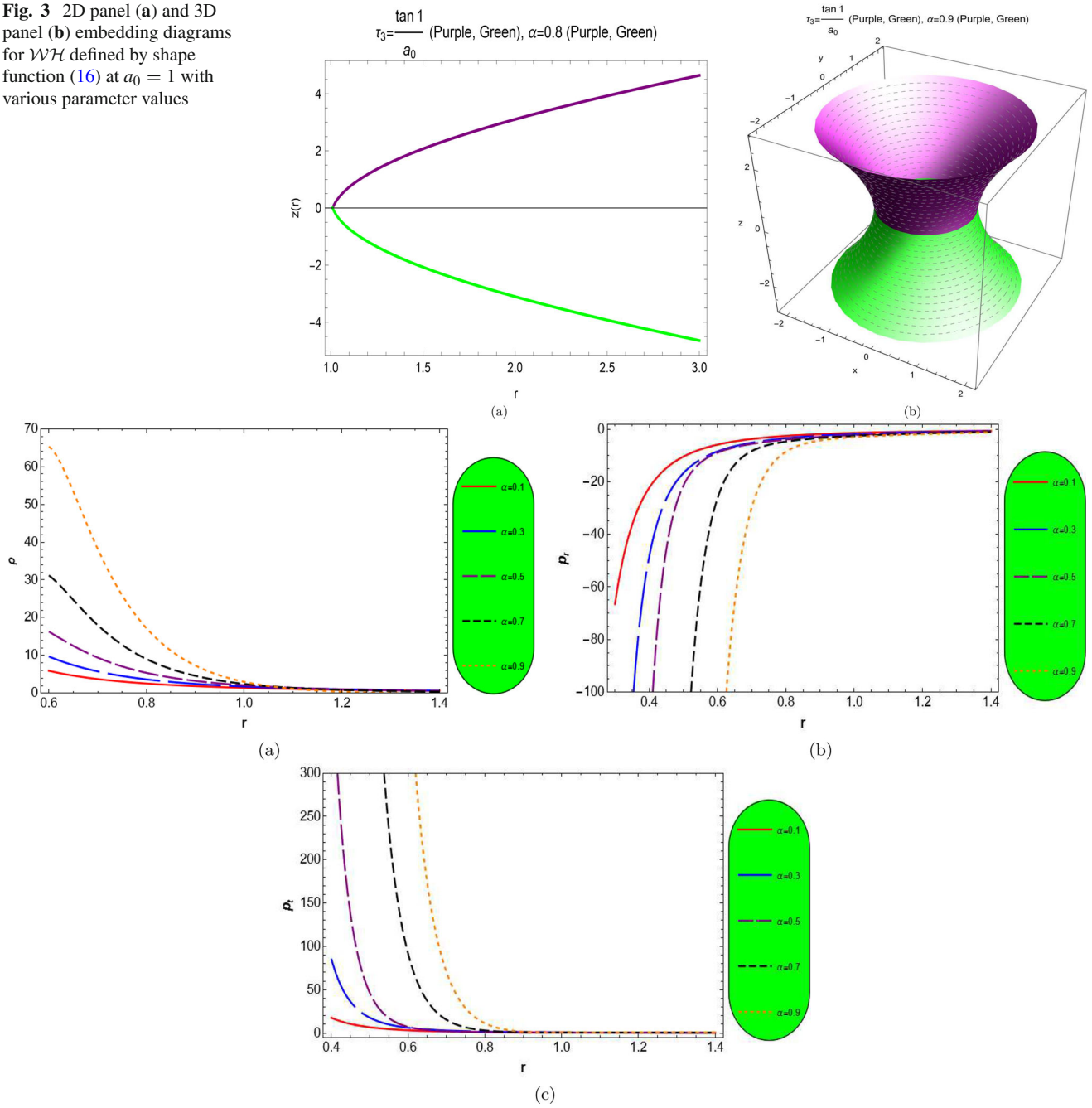

Fig. 3 2D panel (**a**) and 3D panel (**b**) embedding diagrams for $\mathcal{WH}$ defined by shape function (16) at $a_0 = 1$ with various parameter values

Fig. 4 Profiles of ρ panel (**a**), p_r panel (**b**), and p_t panel (**c**) as functions of the radial coordinate r for different values of $\mathcal{GMC}$ $0 < \alpha < 1$, fixed throat radius $a_0 = 1$, and varied correction parameter β and shape function model parameter τ_1

- $\mathcal{WEC}$: $\rho \geq 0$ and $\rho + p_i \geq 0$ which asserts that the energy density measured by any timelike observer is non-negative $T_{\xi\zeta}u^{\xi}u^{\zeta} \geq 0$, where u^{ξ} is a timelike vector, which ensures that observers moving through spacetime will not measure negative energy densities. Violation of this condition implies a breakdown of classical physical expectations and may allow for quantum or non-standard phenomena.
- $\mathcal{SEC}$: $\rho + p_r + 2p_t \geq 0$, this condition requires that the gravitational field should be attractive, i.e., matter should tend to focus geodesics. It appears in the Raychaudhuri equation for timelike geodesic congruences which is often used in singularity theorems and cosmological studies. Its violation is associated with accelerated expansion phases of the universe, such as inflation or $\mathcal{DE}$-dominated epochs.

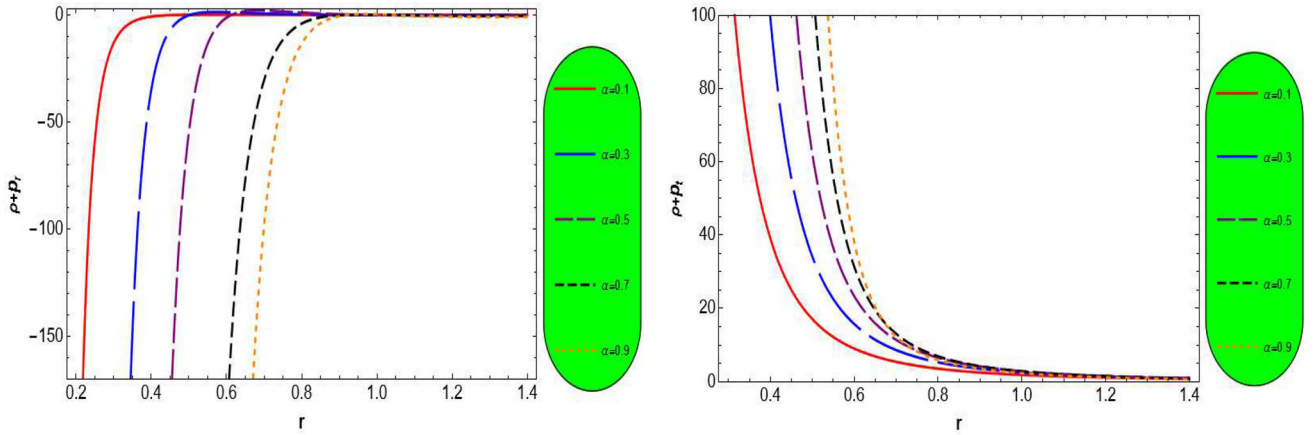

(a) (b)

Fig. 5 Plots of $\rho + p_r$ and $\rho + p_t$ vs. r with $0 < \alpha < 1$ and $a_0 = 1$

- $\mathcal{DEC}$: $\rho \geq |p_i|$, which ensures that the energy flux does not exceed the speed of light, meaning that energy and momentum propagate in a causal (non-spacelike) manner that prevents superluminal propagation of matter and enforces causality in energy transport. Violation of the $\mathcal{DEC}$ could indicate unphysical scenarios such as tachyonic matter or non-causal effects.

We investigate $\mathcal{WH}$ models influenced by $\mathcal{GMC}$ which is a topological defect theorized in gauge theories, while the inclusion of this charge modifies both the spacetime curvature and the energy conditions. By including a $\mathcal{GMC}$, we introduce additional curvature effects that influence the energy conditions and the overall feasibility of the $\mathcal{WH}$.

4.1 Model-1

First shape is defined as $A(r) = \left[1 + \tau_1\left(1 - \frac{a_0}{r}\right)\right]a_0$. The parameters α $\mathcal{GMC}$ parameter and β deviation from $\mathcal{GTR}$ due to $f(R)$ gravity. Now we will discuss the physical properties of traversable $\mathcal{WH}$ under consideration by substituting the shape function into the field equations (11)–(13) yields explicit expressions for ρ, p_r, and p_t.

$$\begin{aligned}\rho = \frac{1}{r^8}\Big[&-12(\tau_1+1)\beta\alpha^2\left(\alpha^2-1\right)a_0r^3\\&+\tau_1\alpha^2a_0^2r^2\left(r^2-12\left(3\beta\alpha^2+\beta\right)\right)\\&-\left(\alpha^2-1\right)r^4\left(2\beta\left(1-5\alpha^2\right)+r^2\right)\\&-62\tau_1^2\beta\alpha^4a_0^4+56\tau_1(\tau_1+1)\beta\alpha^4a_0^3r\Big]\end{aligned} \tag{21}$$

$$\begin{aligned}p_r = \frac{1}{r^8}\Big[&\tau_1\alpha^2a_0^2r^2\left(r^2-4\beta\left(5\alpha^2+3\right)\right)\\&+\left(\alpha^2-1\right)r^4\left(2\left(7\beta\alpha^2+\beta\right)+r^2\right)\\&-(\tau_1+1)\alpha^2a_0r^3\left(12\beta\left(\alpha^2-1\right)+r^2\right)\\&-26\tau_1^2\beta\alpha^4a_0^4+28\tau_1(\tau_1+1)\beta\alpha^4a_0^3r\Big]\end{aligned} \tag{22}$$

$$\begin{aligned}p_t = \frac{1}{2r^8}\Big[&4\beta\left(-7\alpha^4+6\alpha^2+1\right)r^4\\&-2\tau_1\alpha^2a_0^2r^2\left(r^2-8\beta\left(5\alpha^2+3\right)\right)\\&+(\tau_1+1)\alpha^2a_0r^3\left(36\beta\left(\alpha^2-1\right)+r^2\right)\\&+156\tau_1^2\beta\alpha^4a_0^4-140\tau_1(\tau_1+1)\beta\alpha^4a_0^3r\Big]\end{aligned} \tag{23}$$

Figure 4 shows that the energy density ρ remains positive for the chosen ranges of α and β, while the radial pressure p_r is negative and the tangential pressure p_t stays positive, reflecting the anisotropic nature of the $\mathcal{WH}$ matter. We then examine the energy conditions to evaluate the physical viability and stability of the solutions, where the $\mathcal{WEC}$ along the radial and tangential directions is given by $\rho + p_r$ and $\rho + p_t$, respectively.

$$\begin{aligned}\rho + p_r = \frac{1}{r^8}\Big[&\alpha^2\left(24\beta\left(\alpha^2-1\right)r^4\right.\\&+2\tau_1a_0^2r^2\left(r^2-4\beta\left(7\alpha^2+3\right)\right)\\&-(\tau_1+1)a_0r^3\left(24\beta\left(\alpha^2-1\right)+r^2\right)-88\tau_1^2\beta\alpha^2a_0^4\\&\left.+84\tau_1(\tau_1+1)\beta\alpha^2a_0^3r\right)\Big]\end{aligned} \tag{24}$$

$$\begin{aligned}\rho + p_t = \frac{1}{2r^8}\Big[&8\tau_1\beta\alpha^2\left(\alpha^2+3\right)a_0^2r^2\\&-2\left(\alpha^2-1\right)r^4\left(4\beta\left(\alpha^2+1\right)+r^2\right)\\&+(\tau_1+1)\alpha^2a_0r^3\left(12\beta\left(\alpha^2-1\right)+r^2\right)\\&+32\tau_1^2\beta\alpha^4a_0^4-28\tau_1(\tau_1+1)\beta\alpha^4a_0^3r\Big]\end{aligned} \tag{25}$$

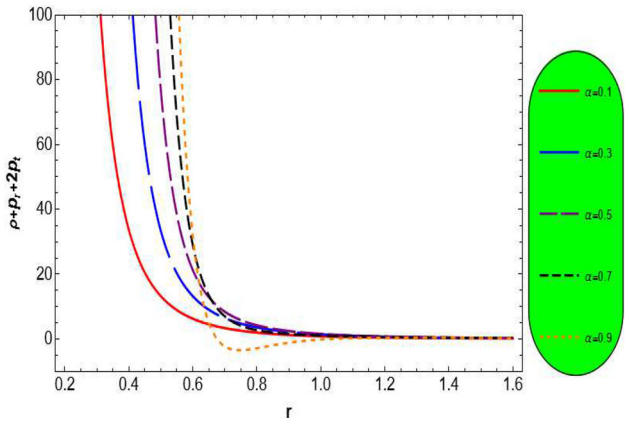

Fig. 6 Plot of $\mathcal{SEC}$ $\rho + p_r + 2p_t$ versus r for $0 < \alpha < 1$, fixed throat radius $a_0 = 1$, and varying correction parameter β and shape function model parameter τ_1

Their variations with respect to the radial coordinate are shown in Fig. 5.

From the plots (Fig. 5), it is evident that the $\mathcal{WEC}$ in the radial direction is violated for certain parameter ranges, which highlights the exotic characteristics of the matter in supporting the $\mathcal{WH}$ structure under these assumptions, while the tangential $\mathcal{WEC}$ remains satisfied throughout the domain. This anisotropic violation suggests that the matter content near the throat does not completely comply with classical energy conditions in the radial direction but behaves normally tangentially. The $\mathcal{SEC}$, defined as $\rho + p_r + 2p_t$, is calculated as

$$\begin{aligned}\rho + p_r + 2p_t = \frac{-1}{r^8}\Big[&4\beta\big((\alpha^4-1)r^4\\ &-3(\tau_1+1)\alpha^2(\alpha^2-1)a_0r^3\\ &-6\tau_1\alpha^2(\alpha^2+1)a_0^2r^2-17\tau_1^2\alpha^4a_0^4\\ &+14\tau_1(\tau_1+1)\alpha^4a_0^3r\big)\Big] \end{aligned} \tag{26}$$

and its behavior is shown in Fig. 6.

The $\mathcal{SEC}$ is seen to be satisfied for all chosen parameters, implying that the combined matter pressures and energy density conform to this condition despite the violations observed in the $\mathcal{WEC}$ along the radial direction. To further examine the $\mathcal{DEC}$, which impose $\rho \geq |p_r|$ and $\rho \geq |p_t|$, we derive:

$$\begin{aligned}\rho - |p_r| = \frac{1}{r^8}\Big[&(\tau_1+1)\alpha^2a_0r^5-16\tau_1\beta\alpha^4a_0^2r^2\\ &-2(\alpha^2-1)r^4\big(2\beta(\alpha^2+1)+r^2\big)-36\tau_1^2\beta\alpha^4a_0^4\\ &+28\tau_1(\tau_1+1)\beta\alpha^4a_0^3r\Big] \end{aligned} \tag{27}$$

$$\begin{aligned}\rho - |p_t| = \frac{-1}{2r^8}\Big[&-4\tau_1\alpha^2a_0^2r^2\big(r^2-2\beta(19\alpha^2+9)\big)\\ &+2(\alpha^2-1)r^4\big(r^2-24\beta\alpha^2\big)+(\tau_1+1)\alpha^2a_0r^3\\ &\times\big(60\beta(\alpha^2-1)+r^2\big)+280\tau_1^2\beta\alpha^4a_0^4\\ &-252\tau_1(\tau_1+1)\beta\alpha^4a_0^3r\Big] \end{aligned} \tag{28}$$

The corresponding graphs for $\mathcal{DEC}$ are presented in Fig. 7. It is evident from Fig. 7 that both forms of $\mathcal{DEC}$ are satisfied, which is consistent with the anisotropic nature of the matter threading the $\mathcal{WH}$.

Consequently, the combined analytical and graphical analyses indicate the existence of $\mathcal{WH}$ solutions with traversable geometry that are influenced by the $\mathcal{GMC}$ and corrections inherent in $f(R)$ gravity, despite partial violations of some classical energy conditions such as the radial $\mathcal{WEC}$ and both $\mathcal{DEC}$s, the tangential $\mathcal{WEC}$ and $\mathcal{SEC}$ remain satisfied, suggesting the presence of non-$\mathcal{EM}$ in the tangential sector. The repulsive anisotropic forces ensure the stability and traversability of the $\mathcal{WH}$. Therefore, such topologically charged $\mathcal{WH}$s can exist without necessarily violating all energy conditions when considering the chosen shape function and the specific physical parameters. This framework provides fertile ground for the construction of physically viable $\mathcal{WH}$ models in $\mathcal{AGT}$s.

4.2 Model-2

The $\mathcal{WH}$ geometry is determined by the shape function $A(r)$, which defines the throat structure and its embedding in spacetime. Here, an exponential form $A(r) = r\,e^{\tau_2(a_0-r)}$ is used [102], providing smooth behavior and controllable throat size a_0 and decay parameter τ_2. This choice facilitates analytic and numerical studies in $f(R)$ gravity. The $\mathcal{EMT}$ components energy density ρ, radial pressure p_r, and tangential pressure p_t describe the anisotropic matter threading the $\mathcal{WH}$ and depend on r, α, β, and τ_2. The exponential terms capture the influence of the topological charge and gravitational modifications and are computed using Eqs. (11)–(13).

$$\begin{aligned}\rho = \frac{1}{r^4}\Big(&-\tau_2\alpha^2r^3e^{\tau_2(a_0-r)}\big(2\tau_2^2\beta\alpha^2\big(3e^{\tau_2(a_0-r)}-2\big)+1\big)\\ &+r^2\big(2\tau_2^2\beta\alpha^4e^{\tau_2(a_0-r)}\big(3e^{\tau_2(a_0-r)}-2\big)\\ &+\alpha^2\big(e^{\tau_2(a_0-r)}-1\big)+1\big)\\ &+8\tau_2\beta\alpha^4re^{\tau_2(a_0-r)}\big(e^{\tau_2(a_0-r)}-1\big)\\ &+2\beta\big(5\alpha^4\big(e^{\tau_2(a_0-r)}-1\big)^2+6\alpha^2\big(e^{\tau_2(a_0-r)}-1\big)+1\big)\Big) \end{aligned} \tag{29}$$

$$\begin{aligned}p_r = \frac{1}{r^4}\Big(&r^2\big(-2\tau_2^2\beta\alpha^4e^{\tau_2(a_0-r)}\big(3e^{\tau_2(a_0-r)}-4\big)\\ &-\alpha^2\big(e^{\tau_2(a_0-r)}-1\big)-1\big)+2\beta\big(7\alpha^4\big(e^{\tau_2(a_0-r)}-1\big)^2\\ &+6\alpha^2\big(e^{\tau_2(a_0-r)}-1\big)-1\big)\Big) \end{aligned} \tag{30}$$

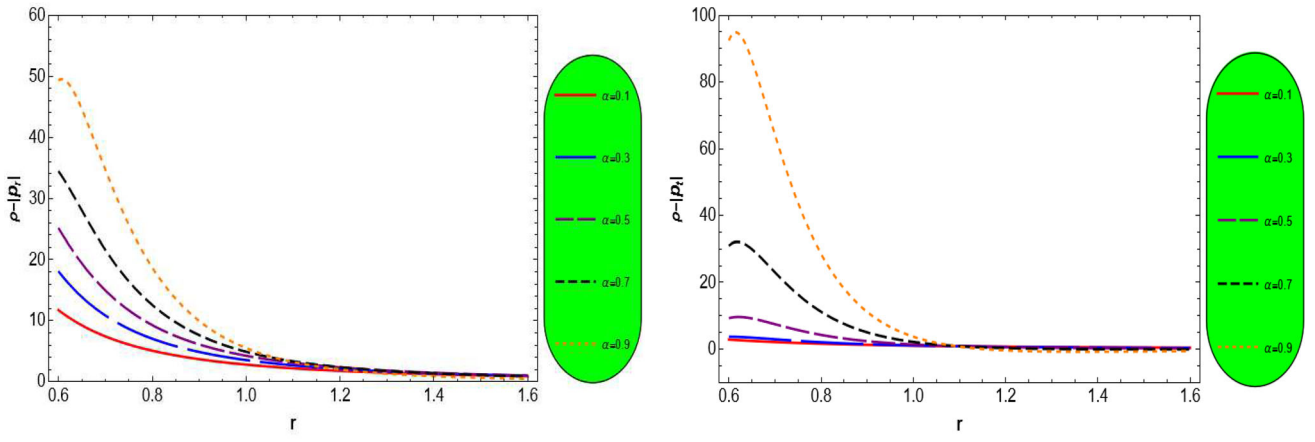

Fig. 7 Graphs of the $\mathcal{DEC}$s $\rho - |p_r|$ (**a**) and $\rho - |p_t|$ (**b**) as functions of r for varying values of $0 < \alpha < 1$, fixed throat radius $a_0 = 1$, $\tau_1 = 0.5$, and different correction parameters and shape function model parameter

$$p_t = \frac{1}{2r^4}\Big(4\beta\big(\alpha^4\big(3\tau_2^3 r^3 - 7\tau_2 r - 7\big)e^{2\tau_2\left(a_0-r\right)} - \alpha^2 e^{\tau_2\left(a_0-r\right)}\big(-14\alpha^2 + 2\tau_2^3\alpha^2 r^3 + \tau_2\big(3-7\alpha^2\big)r + 6\big) - 7\alpha^4 + 6\alpha^2 + 1\big) + \tau_2\alpha^2 r^3 e^{\tau_2\left(a_0-r\right)}\Big) \tag{31}$$

For a fixed throat radius $a_0 = 1$, we examine the physical variables for a range of the $\mathcal{GMC}$ $0 < \alpha < 1$ and different values of the $f(R)$ correction parameter β to capture the influence of topological and $\mathcal{AGT}$ effects.

Physical analysis and graphical interpretation

- Energy density: The behavior of ρ as depicted in Fig. 8(a) indicates that it remains positive for select values of α τ_2 and β. For larger choices, notably $\alpha = 0.77$ and $\alpha = 0.99$, ρ may become negative in certain regions, highlighting the sensitivity of the energy density to the $\mathcal{GMC}$ in this model.
- Radial and tangential pressures: The profiles displayed in Fig. 8(b)–(c) reveal that p_r remains negative, indicating tension along the radial direction, while p_t is consistently positive, suggesting repulsive behavior in the transverse directions.

Plots (Fig. 8) for ρ, p_r and p_t are as:

The fundamental energy conditions are evaluated as follows: The expression for $\mathcal{WEC}$ under the influence of the considered shape function is:

$$\rho + p_r = -\frac{1}{r^4}\Big(\alpha^2\big(2\beta\alpha^2\big(3\tau_2^3 r^3 - 4\tau_2 r - 12\big)e^{2\tau_2\left(a_0-r\right)} + e^{\tau_2\left(a_0-r\right)}\big(24\beta\big(2\alpha^2-1\big) + r^3\big(\tau_2 - 4\tau_2^3\beta\alpha^2\big) - 4\tau_2^2\beta\alpha^2 r^2 + 8\tau_2\beta\alpha^2 r\big) - 24\beta\big(\alpha^2-1\big)\big)\Big) \tag{32}$$

$$\rho + p_t = -\frac{1}{2r^4}\Big(\tau_2\alpha^2 r^3 e^{\tau_2\left(a_0-r\right)} - 2r^2\big(2\tau_2^2\beta\alpha^4 e^{\tau_2\left(a_0-r\right)}\big(3e^{\tau_2\left(a_0-r\right)} - 2\big) + \alpha^2\big(e^{\tau_2\left(a_0-r\right)} - 1\big) + 1\big) + 8\beta\big(\alpha^4\big(e^{\tau_2\left(a_0-r\right)} - 1\big)^2 - 1\big) + 12\tau_2\beta\alpha^2 r e^{\tau_2\left(a_0-r\right)}\big(\alpha^2\big(e^{\tau_2\left(a_0-r\right)} - 1\big) + 1\big)\Big) \tag{33}$$

Plots (Fig. 9) for fixed value of throat radius are given below:

The $\mathcal{WEC}$ involves $\rho + p_r$ and $\rho + p_t$, measuring whether observed matter is effectively non-exotic in the radial and tangential directions. In our case study, the $\mathcal{WEC}$ in the radial direction is generally violated throughout the range of parameters explored, while its tangential component is fulfilled for the admissible values of α and β. This dynamic reflects the delicate energy support required for traversable $\mathcal{WH}$s under these gravitational modifications. The $\mathcal{SEC}$ combines $\rho + p_r + 2p_t$, reflecting the tendency of matter to focus on geodesics and contribute attractively to gravity, and the $\mathcal{SEC}$s can be obtained in the following form:

$$\rho + p_r + 2p_t = \frac{1}{r^4}\Big(2\beta\big(\alpha^4\big(3\tau_2^3 r^3 - 10\tau_2 r - 2\big)e^{2\tau_2\left(a_0-r\right)} + e^{\tau_2\left(a_0-r\right)}\big(4\alpha^4 - 2\tau_2^3\alpha^4 r^3 + 2\tau_2^2\alpha^4 r^2 + 2\tau_2\big(5\alpha^2-3\big)\alpha^2 r\big) - 2\alpha^4 + 2\big)\Big) \tag{34}$$

The plots for $\mathcal{SEC}$s are:

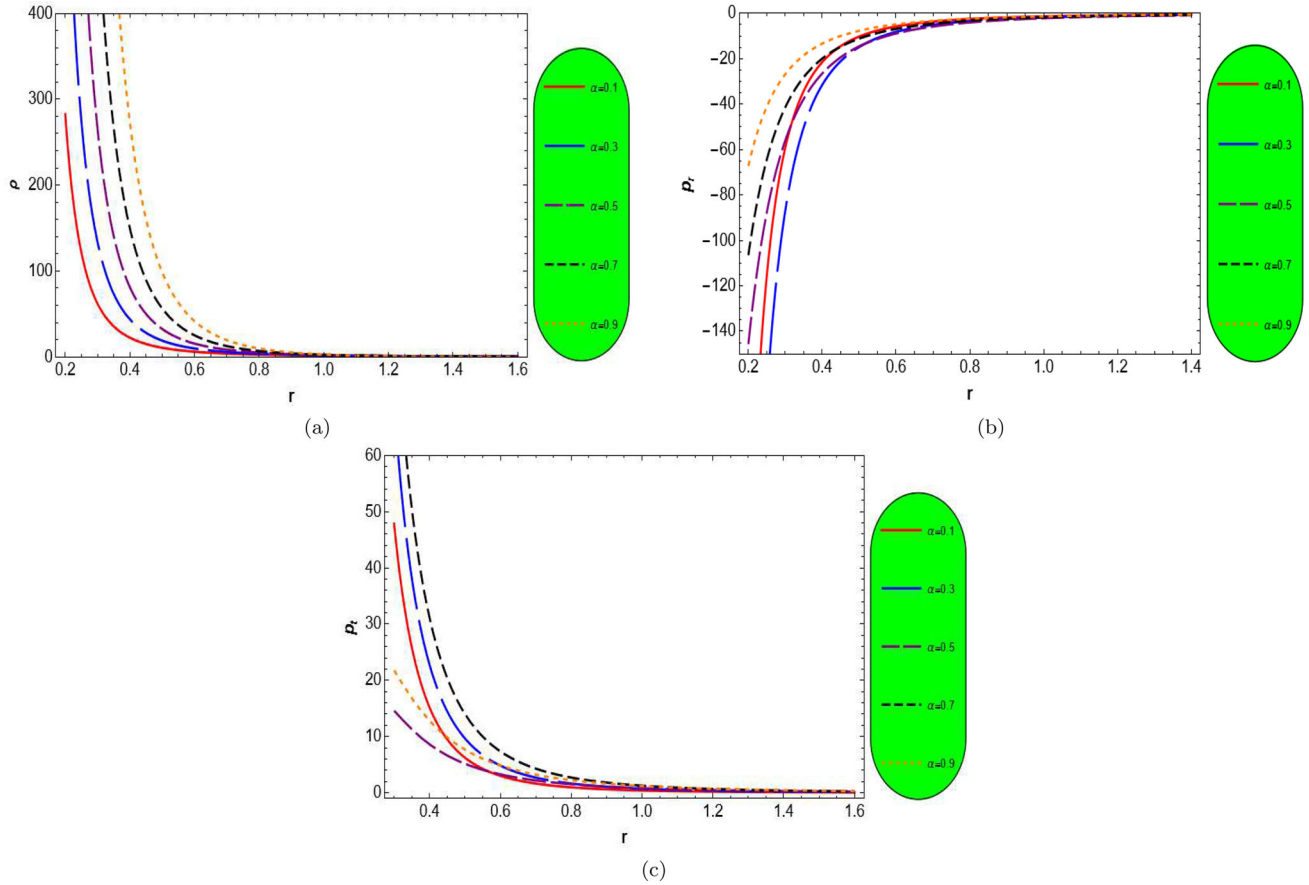

Fig. 8 Graphs of ρ, p_r, and p_t vs. r for various values of α τ_2 and β with fixed $a_0 = 1$

The $\mathcal{SEC}$ is satisfied for all considered values of α and β, which can be seen from Fig. 10, confirming that the spacetime supports matter distributions that obey the strong gravitational focusing condition. The $\mathcal{DEC}$ constraints, $\rho - |p_r|$ and $\rho - |p_t|$, ensure causality and physically reasonable propagation speeds for energy flow, while these conditions in this model come up with the equations below:

$$\begin{aligned}\rho - |p_r| = \frac{1}{r^4}\Big(& -\tau_2\alpha^2 r^3 e^{\tau_2(a_0-r)}\left(2\tau_2^2\beta\alpha^2\left(3e^{\tau_2(a_0-r)}-2\right)+1\right)\\ & +2r^2\left(6\tau_2^2\beta\alpha^4 e^{\tau_2(a_0-r)}\left(e^{\tau_2(a_0-r)}-1\right)\right.\\ & \left.+\alpha^2\left(e^{\tau_2(a_0-r)}-1\right)+1\right)\\ & +8\tau_2\beta\alpha^4 r e^{\tau_2(a_0-r)}\left(e^{\tau_2(a_0-r)}-1\right)\\ & -4\beta\left(\alpha^4\left(e^{\tau_2(a_0-r)}-1\right)^2-1\right)\Big) \end{aligned} \tag{35}$$

$$\begin{aligned}\rho - |p_t| = \frac{1}{2r^4}\Big(& \tau_2\alpha^2 r^3\left(-e^{\tau_2(a_0-r)}\right)\left(8\tau_2^2\beta\alpha^2\left(3e^{\tau_2(a_0-r)}\right.\right.\\ & \left.-2\right)+3\Big)+2r^2\left(2\tau_2^2\beta\alpha^4 e^{\tau_2(a_0-r)}\left(3e^{\tau_2(a_0-r)}-2\right)\right.\\ & \left.+\alpha^2\left(e^{\tau_2(a_0-r)}-1\right)+1\right)\\ & +4\tau_2\beta\alpha^2 r e^{\tau_2(a_0-r)}\left(11\alpha^2\left(e^{\tau_2(a_0-r)}-1\right)+3\right)\\ & +48\beta\alpha^2\left(e^{\tau_2(a_0-r)}-1\right)\\ & \times\left(\alpha^2\left(e^{\tau_2(a_0-r)}-1\right)+1\right)\Big) \end{aligned} \tag{36}$$

The graphs generated can be seen below:

Inspection of $\mathcal{DEC}$ plots (Fig. 11) shows that satisfaction of the constraint is achieved. The results of this exponential shape function model demonstrate the intricate balance between the energy conditions and the physical viability of traversable $\mathcal{WH}$ geometries in $f(R)$ gravity. The energy density can span negative and positive values depending on the $\mathcal{GMC}$, whereas pressures exhibit clear anisotropy.

4.3 Model-3

Now consider a shape function of the form [102]: $A(r) = a_0 \tan^{-1}(\tau_3 r)$ which ensures smooth behavior near the throat and suitable asymptotic characteristics, facilitating analytical tractability within the context of $f(R)$ gravity influenced by a $\mathcal{GMC}$. Using Eqs. (11)–(13), we compute the energy density ρ, radial pressure p_r, and tangential pressure p_t and the resulting expressions, though complex, capture the depen-

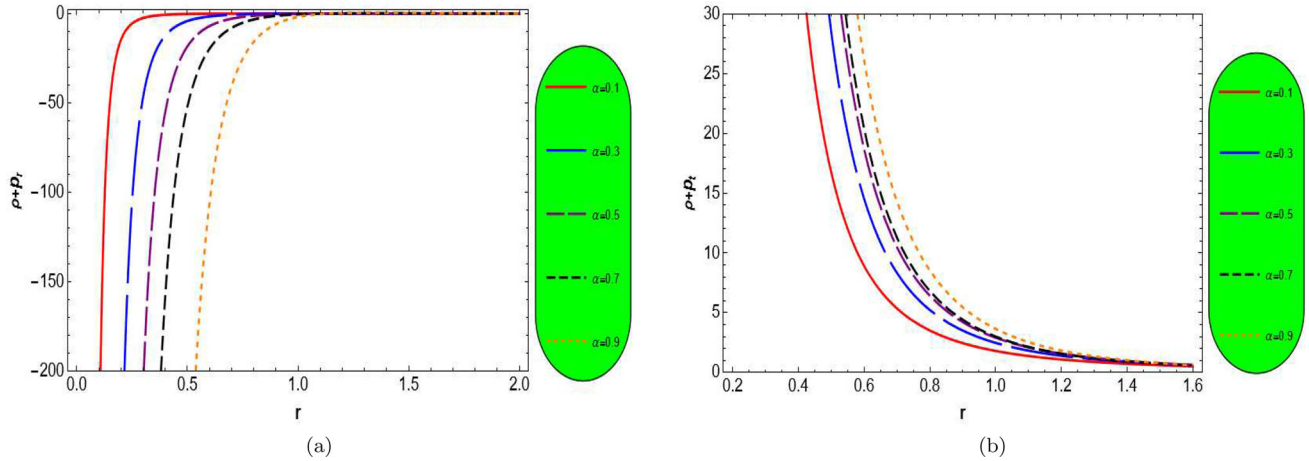

Fig. 9 Diagrams of both $\rho + p_r$ and $\rho + p_t$ vs. r with specific range of α and β

dence on α, β, and r as follows:

$$\rho = \frac{1}{r^5\left(\tau_3^2 r^2+1\right)^3}\Big(2a_0^2\tau_3\beta\alpha^4\big(2\big(14\tau_3^4 r^4 + 9\tau_3^2 r^2+3\big)\tan^{-1}(\tau_3 r) - \tau_3 r\big(3\tau_3^2 r^2+1\big)\big) + a_0\alpha^2\big(\tau_3 r\big(\tau_3^4 r^6 + r^2\big(1-24\tau_3^2\beta\alpha^2\big) + r^4\big(2\tau_3^2-48\tau_3^4\beta\alpha^2\big) - 8\beta\alpha^2\big) - 12\beta\big(\alpha^2-1\big)\big(\tau_3^2 r^2+1\big)^3\tan^{-1}(\tau_3 r)\big) - \big(\alpha^2-1\big) \times r\big(\tau_3^2 r^2+1\big)^3\big(2\beta\big(1-5\alpha^2\big)+r^2\big)\Big) \tag{37}$$

$$p_r = \frac{1}{r^5}\Bigg(\frac{r}{\left(\tau_3^2 r^2+1\right)^2}\Big(2a_0^2\tau_3^2\beta\alpha^4 - 16a_0\tau_3\beta\alpha^4\big(2\tau_3^2 r^2+1\big) + \big(\alpha^2-1\big)\big(\tau_3^2 r^2+1\big)^2\big(2\big(7\beta\alpha^2+\beta\big)+r^2\big)\Big) + a_0\alpha^2\tan^{-1}(\tau_3 r)\Big(\frac{4a_0\tau_3\beta\alpha^2\big(7\tau_3^2 r^2+3\big)}{\left(\tau_3^2 r^2+1\right)^2} - 12\beta\big(\alpha^2-1\big) - r^2\Big)\Bigg) \tag{38}$$

$$p_t = \frac{1}{2r^5\left(\tau_3^2 r^2+1\right)^3}\Big(-4a_0^2\tau_3\beta\alpha^4\big(\big(35\tau_3^4 r^4 + 28\tau_3^2 r^2+9\big)\tan^{-1}(\tau_3 r) - 2\tau_3 r\big(2\tau_3^2 r^2+1\big)\big) + a_0\alpha^2\big(\big(\tau_3^2 r^2+1\big)^3 \times \tan^{-1}(\tau_3 r)\big(36\beta\big(\alpha^2-1\big)+r^2\big) + \tau_3 r\big(-\tau_3^4 r^6 + 2\tau_3^2 r^4\big(2\tau_3^2\beta\big(29\alpha^2+3\big)-1\big) + r^2\big(24\tau_3^2\big(3\beta\alpha^2+\beta\big)-1\big) + 4\beta\big(5\alpha^2+3\big)\big)\big) - 4\beta\big(7\alpha^4-6\alpha^2-1\big)r\big(\tau_3^2 r^2+1\big)^3\Big) \tag{39}$$

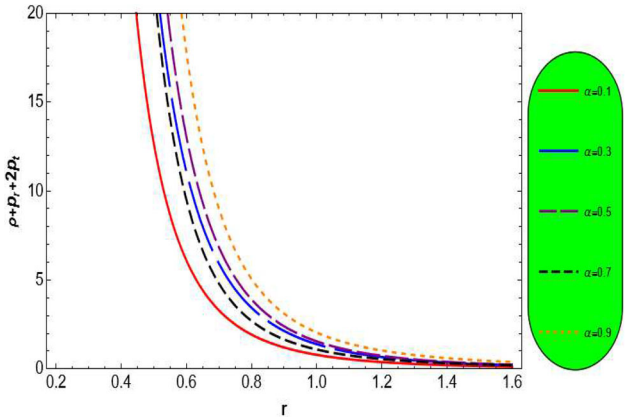

Fig. 10 Graph for $\rho + p_r + 2p_t$ vs. r for several α and β

For a complete understanding, we analyze numerical graphs of ρ, p_r, and p_t versus the radial coordinate r, fixing the radius of the throat at $a_0 = 1$, some values of the parameter τ_3, and varying the $\mathcal{GMC}$ α and the correction parameter β within the physically relevant ranges $0 < \alpha < 1$.

From Fig. 12, it is evident that:

- The energy density ρ remains positive in certain parameter regimes, indicating possible physical viability in these cases.
- The radial pressure p_r is negative throughout the domain, implying radial tension at the throat, a common characteristic in $\mathcal{WH}$ matter profiles.
- The tangential pressure p_t remains positive, signifying repulsive transverse stresses that potentially stabilize the structure of the $\mathcal{WH}$.

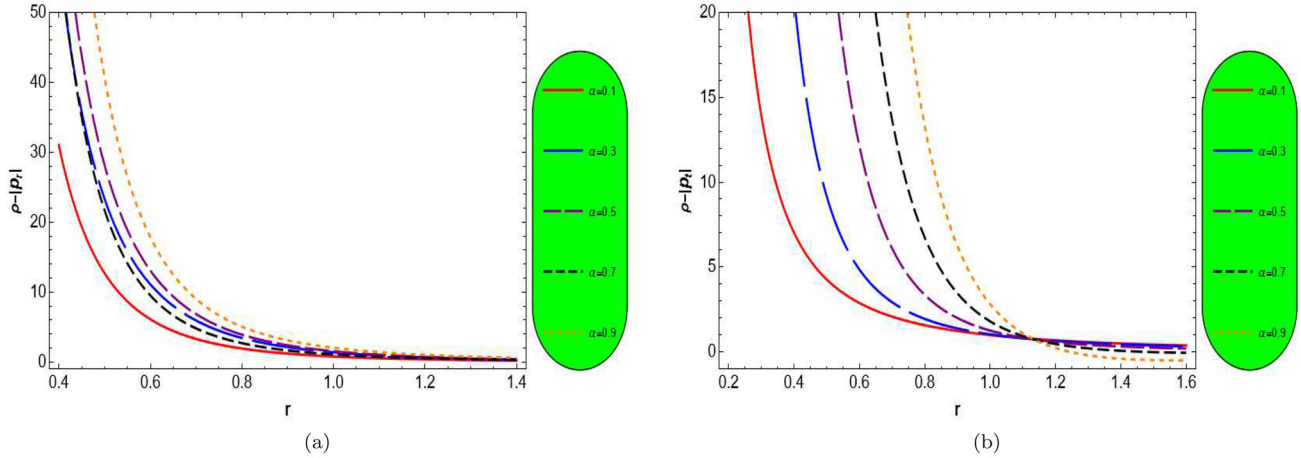

Fig. 11 Plots of $\rho - |p_r|$ and $\rho - |p_t|$ in panels (**a**) and (**b**) for specific ranges of α and β considered

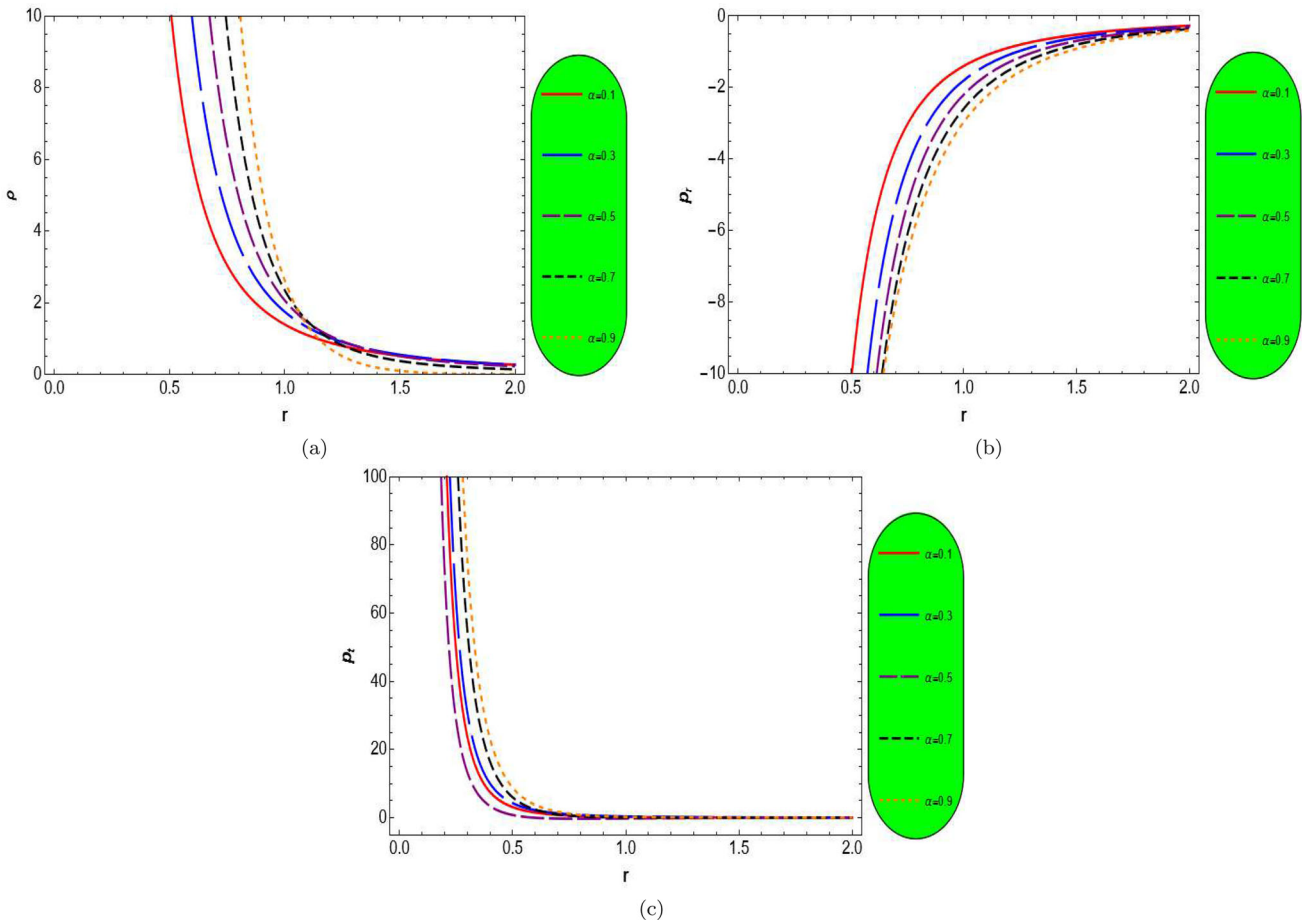

Fig. 12 Graphs of physical entities for ρ, p_r, p_t in panels (**a**), (**b**) and (**c**), respectively, as function of r for different values of $\mathcal{GMC}$ $0 < \alpha < 1$, throat radius $a_0 = 1$, some values of τ_3 and different values of correction parameter β

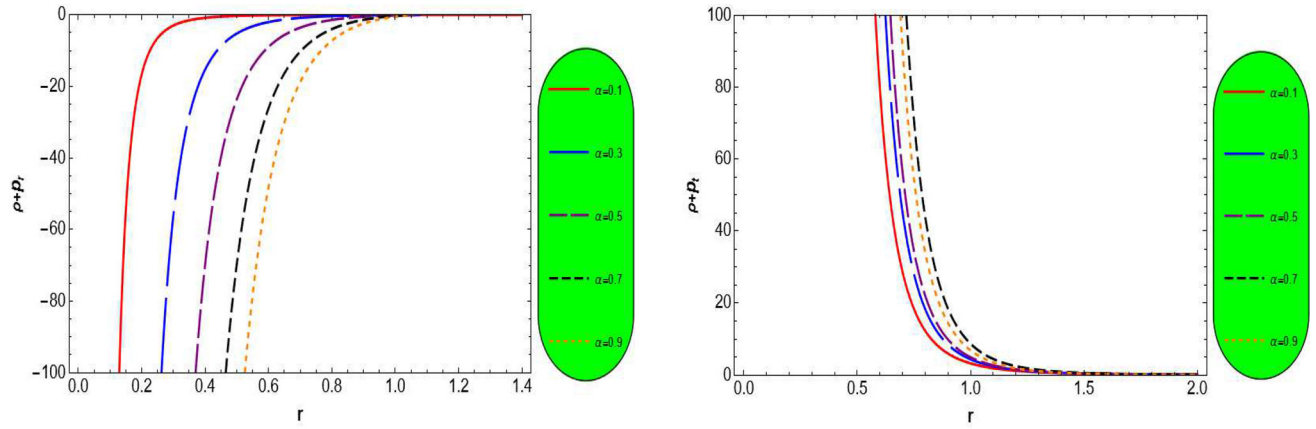

Fig. 13 $\rho + p_r$, $\rho + p_t$, in panels (**a**), (**b**), respectively, as function of r for different values of $\mathcal{GMC}$ $0 < \alpha < 1$, throat radius $a_0 = 1$, and some values of τ_3

The $\mathcal{WEC}$s yield the following expressions:

$$\begin{aligned}\rho + p_r = {} & \frac{1}{r^5\left(\tau_3^2 r^2+1\right)^3}\Big(\alpha^2\big(-a_0\left(\left(\tau_3^2 r^2+1\right)^3\right.\\ & \times \tan^{-1}(\tau_3 r)\left(24\beta\left(\alpha^2-1\right)+r^2\right)\\ & -\tau_3 r\left(\tau_3^4 r^6+r^2\left(1-72\tau_3^2\beta\alpha^2\right)\right.\\ & +r^4\left(2\tau_3^2-80\tau_3^4\beta\alpha^2\right)-24\beta\alpha^2\big)\big)\\ & +4a_0^2\tau_3\beta\alpha^2\left(\left(21\tau_3^4 r^4+19\tau_3^2 r^2+6\right)\tan^{-1}(\tau_3 r)\right.\\ & \left.\left.-\tau_3^3 r^3\right)+24\beta\left(\alpha^2-1\right)r\left(\tau_3^2 r^2+1\right)^3\right)\Big) \qquad (40)\end{aligned}$$

$$\begin{aligned}\rho + p_t = {} & \frac{1}{2r^5\left(\tau_3^2 r^2+1\right)^2}\Big(-4a_0^2\tau_3\beta\alpha^4\left(\left(7\tau_3^2 r^2+3\right)\right.\\ & \times \tan^{-1}(\tau_3 r)-\tau_3 r\big)+a_0\alpha^2\left(\left(\tau_3^2 r^2+1\right)^2\right.\\ & \times \tan^{-1}(\tau_3 r)\left(12\beta\left(\alpha^2-1\right)+r^2\right)\\ & +\tau_3 r\left(\tau_3^2 r^4+r^2\left(4\tau_3^2\beta\left(5\alpha^2+3\right)+1\right)\right.\\ & \left.\left.+4\beta\left(\alpha^2+3\right)\right)\right)-2\left(\alpha^2-1\right)r\left(\tau_3^2 r^2+1\right)^2\\ & \left.\left(4\beta\left(\alpha^2+1\right)+r^2\right)\Big) \qquad (41)\end{aligned}$$

A graphical visualization for $\mathcal{WEC}$s is as follows:

As depicted in Fig. 13, the radial component of the $\mathcal{WEC}$ is generally violated for the parameter ranges considered, whereas the tangential $\mathcal{WEC}$ condition is satisfied consistently, reflecting anisotropic energy distributions that sometimes mimic non-$\mathcal{EM}$ behaviors. The equation describing the physical constraint of $\mathcal{SEC}$ results:

$$\begin{aligned}\rho + p_r + 2p_t = {} & -\frac{1}{r^5\left(\tau_3^2 r^2+1\right)^3}\Big(4\beta\big(a_0^2\tau_3\alpha^4\left(\left(14\tau_3^4 r^4\right.\right.\\ & \left.+9\tau_3^2 r^2+3\right)\tan^{-1}(\tau_3 r)-\tau_3 r\left(3\tau_3^2 r^2+2\right)\big)\\ & -a_0\alpha^2\left(3\left(\alpha^2-1\right)\right.\\ & \times\left(\tau_3^2 r^2+1\right)^3\tan^{-1}(\tau_3 r)\\ & +\tau_3 r\left(3\tau_3^4\left(3\alpha^2+1\right)r^4+6\tau_3^2 r^2-\alpha^2+3\right)\big)\\ & \left.+\left(\alpha^4-1\right)r\left(\tau_3^2 r^2+1\right)^3\right)\Big) \qquad (42)\end{aligned}$$

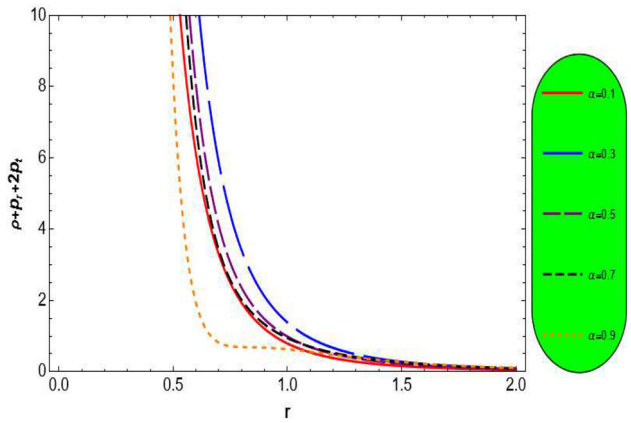

Fig. 14 $\rho + p_r + 2p_t$ versus r for different values of $\mathcal{GMC}$ $0 < \alpha < 1$, throat radius $a_0 = 1$, τ_3

The plots for $\mathcal{SEC}$s are:

The graphical analysis in Fig. 14 indicates that the $\mathcal{SEC}$ is satisfied throughout the parameter space considered, suggesting gravitational focusing behavior consistent with physically reasonable matter fields.

The $\mathcal{DEC}$s in this model, i.e., $\rho - |p_r|$ and $\rho - |p_t|$, are computed as:

$$\begin{aligned}\rho - |p_r| = {} & \frac{1}{r^4\left(\tau_3^2 r^2+1\right)^3}\Big(4a_0^2\tau_3^2\beta\alpha^4\left(-2\tau_3^2 r^2\right.\\ & \left.+\tau_3 r\left(7\tau_3^2 r^2-1\right)\tan^{-1}(\tau_3 r)-1\right)\\ & +a_0\alpha^2\left(r\left(\tau_3^2 r^2+1\right)^3\tan^{-1}(\tau_3 r)\right.\end{aligned}$$

$$+\tau_3\left(\tau_3^4 r^6 + r^2\left(24\tau_3^2\beta\alpha^2+1\right) + r^4\left(2\tau_3^2 - 16\tau_3^4\beta\alpha^2\right) + 8\beta\alpha^2\right) - 2\left(\alpha^2-1\right)\left(\tau_3^2 r^2+1\right)^3 \left(2\beta^2+1\right)+r^2\Big)\Big) \tag{43}$$

$$\rho - |p_t| = -\frac{1}{2r^5\left(\tau_3^2 r^2+1\right)^3}\Big(-4a_0^2\tau_3\beta\alpha^4\big(\big(63\tau_3^4 r^4 + 46\tau_3^2 r^2 + 15\big)\tan^{-1}(\tau_3 r) - \tau_3 r\left(7\tau_3^2 r^2+3\right)\big) + a_0\alpha^2\big(\left(\tau_3^2 r^2+1\right)^3 \times \tan^{-1}(\tau_3 r)\big(60\beta\left(\alpha^2-1\right)+r^2\big) + \tau_3 r\big(-3\tau_3^4 r^6 + 2\tau_3^2 r^4\left(2\tau_3^2\beta\left(53\alpha^2+3\right)-3\right) + 3r^2\left(8\tau_3^2\left(5\beta\alpha^2+\beta\right)-1\right) + 12\left(3\beta\alpha^2+\beta\right)\big)\big) + 2\left(\alpha^2-1\right)r\left(\tau_3^2 r^2+1\right)^3 \left(r^2-24\beta\alpha^2\right)\Big)\Big) \tag{44}$$

The graphs generated can be seen below:

The results in Fig. 15 reveal that the radial $\mathcal{DEC}$ is violated across the parametric domain examined, while the tangential $\mathcal{DEC}$ is fully satisfied, reflecting the constraints of anisotropic causal matter in the $\mathcal{WH}$ environment.

This model demonstrates that $\mathcal{WH}$ geometries with the chosen arctangent shape function can support matter distributions complying with the strong energy condition and exhibiting anisotropy favoring throat stability. However, violations of radial $\mathcal{WEC}$ and $\mathcal{DEC}$ indicate the need for exotic or quasi-$\mathcal{EM}$, albeit with partially non-exotic behavior in tangential directions.

5 Stability analysis

In the context of $\mathcal{GTR}$ and $\mathcal{AGT}$s, a thorough analysis of stability corroborates the viability of equilibrium models, as a physically realistic stellar model must remain in a stable equilibrium state under small perturbation in physical parameters. To examine stability techniques widely employed for systematic and mathematically exploration of how compact stars respond to internal or external disturbances, ensuring the reliability of inferred physical properties [103–111]. Moreover, in our case study, we consider $\mathcal{AGT}$s like $f(R)$ gravity model. The stability criteria often depend sensitively on the choice of EoS, some fix conditions at boundary surface, and considered model of theory, while studies demonstrated that variations in local energy density, anisotropic pressures, and curvature corrections can substantially alter the stability behavior of a compact system. In the subsequent sections, we will analyze the specific stability conditions relevant to our model, employing different tools, which include a discussion on the behavior of Γ, the sound speed constraints and Herrera cracking criterion under the influence of $\mathcal{AGT}$ corrections. These analyses will help establish the range of physical parameters for which the compact configuration remains stable and physically tenable.

5.1 Stability through causality conditions

The principle of causality, a foundational postulate in both classical and relativistic physics, dictates that no signal or information can propagate faster than the speed of light in vacuum. While, one can say in the context of relativistic stellar structures, this principle translates into a critical constraint on the propagation speeds of perturbations specifically, the radial and tangential sound speeds within the matter distribution of compact stars [112,113]. Mathematically, the causality condition [112,113] is enforced by requiring that the squared sound speeds remain bounded within the interval [0, 1], i.e.,

$$0 \leq V_r^2 \leq 1, \quad 0 \leq V_t^2 \leq 1, \tag{45}$$

where $V_r^2 = \frac{dp_r}{d\rho}$ is squared speeds of sound in radial and $V_t^2 = \frac{dp_t}{d\rho}$ is the squared speeds of sound in the tangential directions. These derivatives are taken under the assumption of adiabatic and reversible processes, and they quantify the rate at which pressure responds to density variations under infinitesimal perturbations. From a physical standpoint, the condition $0 \leq V_r^2, V_t^2 \leq 1$ ensures that the local material response to pressure fluctuations remains subluminal and therefore compatible with relativistic causality, while the violations of this constraint would imply either non physical behavior (e.g., negative sound speeds) or superluminal signal propagation, both of which are unacceptable in a realistic stellar model.

In the current analysis with Starobinsky model corrections and $\mathcal{GMC}$, the behavior of V_r^2 and V_t^2 is thoroughly examined for all admissible values of the parameters. The corresponding plots (see Fig. 16) illustrate that both the radial and tangential sound speeds consistently remain within the causal bounds throughout the stellar interior, which strongly supports the physical acceptability and stability of the proposed configurations under the causality criterion. Moreover, it is noteworthy that the radial sound speed typically plays a more dominant role in governing the dynamical stability against radial oscillations, while the tangential component becomes significant in the presence of anisotropic pressure distributions.

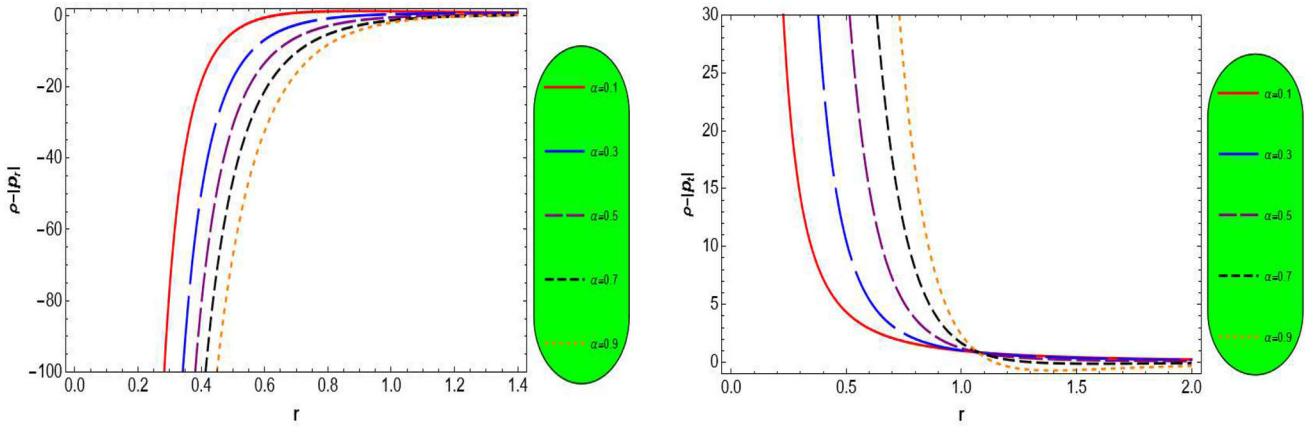

Fig. 15 Graphs of physical entities for $\rho - |p_r|$, $\rho - |p_t|$, in panels (**a**), (**b**), respectively, as function of r for different values of $\mathcal{GMC}$ $0 < \alpha < 1$, throat radius $a_0 = 1$, some values of τ_3 and different values of correction parameter

5.2 Herrera cracking criterion

To assessing the stability of anisotropic stellar configurations is provided by the concept of cracking (also referred to as overturning), initially introduced by Herrera [114], which offers a valuable diagnostic for detecting regions within a compact object that may become unstable due to anisotropic stresses. Herrera's analysis revealed that stability against cracking can be achieved if the absolute difference between the squares of the tangential and radial sound speeds remains bounded by unity [114,115] :

$$\left|V_t^2 - V_r^2\right| \leq 1. \tag{46}$$

Physically, this condition ensures that the anisotropic stresses do not induce significant internal imbalances, which could otherwise prompt the material layers to accelerate away from one another indicating a breakdown of stability, thus, evaluating the variation of $\left|V_t^2 - V_r^2\right|$ across the stellar interior is a robust method for identifying stable versus unstable regions under small non equilibrium perturbations.

In the context of our present model, we computed and plotted the quantity $\left|V_t^2 - V_r^2\right|$ as a function of the radial coordinate for the considered toy models of shape function in the background of $f(R)$ gravity. As illustrated in Fig. 17, the absolute difference remains strictly within the unit interval for all physically acceptable values of the model parameters, which indicates that no cracking or overturning occurs throughout the stellar interior, affirming the dynamical stability of the solutions under anisotropic perturbations. Moreover, the cracking criterion is particularly insightful in anisotropic frameworks where radial and tangential pressures deviate significantly, conditions that are prevalent in realistic models of ultra-dense stellar matter.

5.3 Adiabatic index approach

The adiabatic index a fundamental parameter in the investigation of dynamical stability of stellar objects, which quantifies the stiffness of the EoS of compact fluid under consideration. Physically, it reflects the pressure response of the matter content to adiabatic changes in the energy density, offering critical insight into the tendency of the configuration to equilibrium or gravitational collapse [116,117].

In its classical formulation for isotropic systems, the critical threshold for stability is given by $\Gamma > \frac{4}{3}$, where Γ denotes the adiabatic index. If Γ falls below this critical value, the pressure is insufficient to counteract the gravitational pull, and the compact system becomes dynamically unstable, ultimately leading to collapse. Conversely, values exceeding $4/3$ suggest that the fluid possesses adequate internal pressure to resist compression, thereby indicating stability. Thus, generalized expressions for the anisotropic case are given as [116,117]

$$\Gamma_r = \frac{\rho + p_r}{p_r}\left(\frac{dp_r}{d\rho}\right), \qquad \Gamma_t = \frac{\rho + p_t}{p_t}\left(\frac{dp_t}{d\rho}\right), \tag{47}$$

The terms Γ_r and Γ_t correspond to the adiabatic indices in the radial and tangential directions, respectively, which provide a more complete description of the fluid's compressibility and stability under anisotropic stresses. In particular, the radial index Γ_r is crucial for assessing the stability against radial oscillations, typically the dominant mode of collapse in compact stars, while Γ_t offers additional insight into anisotropic stress responses.

In the present work:

- We evaluated both Γ_r and Γ_t throughout the stellar interior for the considered configurations within $f(R)$ grav-

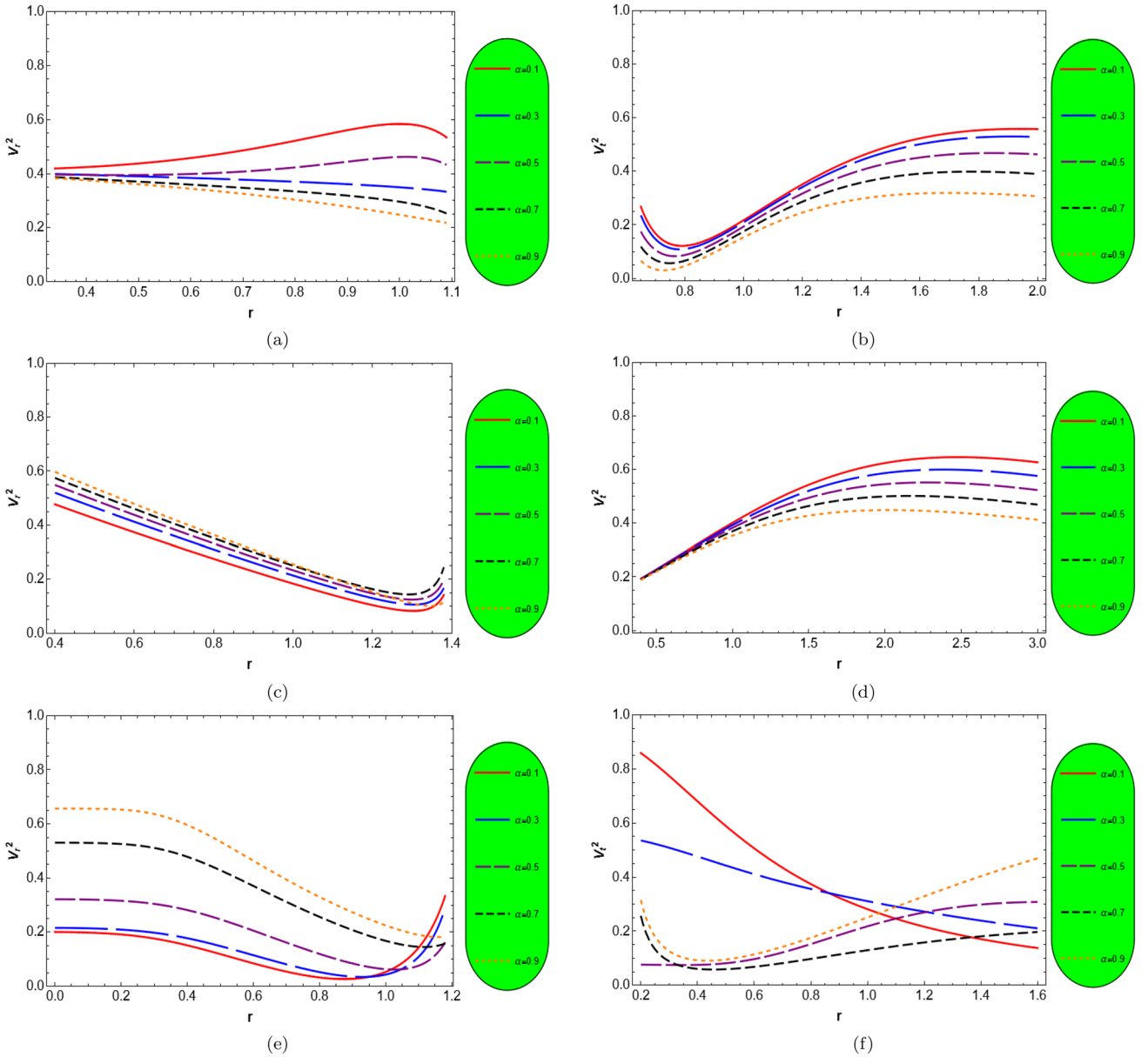

Fig. 16 Profile of causality corresponding to model-1 in panels (**a**), (**b**), for model-2 in panels (**c**), (**d**), and for model-3 in panels (**e**), (**f**) respectively, as function of r for different values of $\mathcal{GMC}$ $0 < \alpha < 1$, throat radius $a_0 = 1$ and different values of correction parameter β along with some values of model parameters τ_1, τ_2, and τ_3

ity. The graphical behavior of these indices is presented in Fig. 18, which demonstrates that both quantities remain strictly greater than the critical value of $4/3$ for possible suitable parameter choices and throughout the entire radial domain, which unequivocally indicates that the proposed stellar models are dynamically stable under adiabatic perturbations.

- Moreover, the monotonicity and positivity of Γ_r and Γ_t further support the absence of instability triggering gradients within the fluid configuration. This analysis, in conjunction with other stability diagnostics such as the causality and cracking conditions, provides a robust confirmation of the internal consistency and physical viability of the proposed anisotropic compact stars.

Anisotropy critically influences $\mathcal{WH}$ stability and traversability in both $\mathcal{GTR}$ and $\mathcal{AGT}$, while we analyze its role in three $\mathcal{WH}$ models. The anisotropy parameter mathematically described as

$$\Delta(r) = p_t(r) - p_r(r).$$

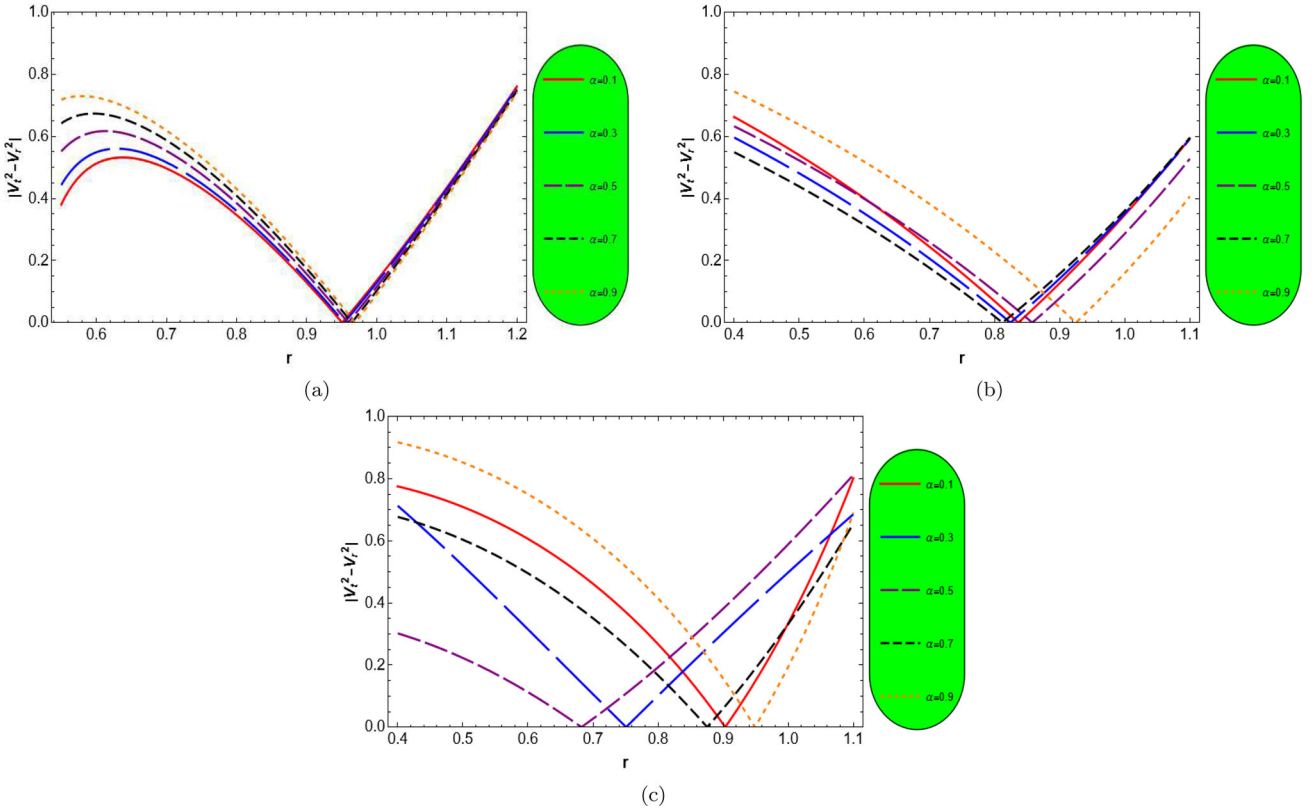

Fig. 17 Graphs of cracking corresponding to model-1 in panels (**a**), for model-2 in panels (**b**), and model-3 in panels (**c**), respectively, as function of r for different values of $\mathcal{GMC}$ $0 < \alpha < 1$, throat radius $a_0 = 1$ and different values of correction parameter β along with some values of model parameters τ_1, τ_2, and τ_3

This relation indicates the pressure difference along tangential and radial directions, so one can conclude three cases: if $\Delta(r) < 0$, this condition indicate radial pressure dominates, producing an inward (attractive) force that may collapse the throat. If $\Delta(r) > 0$, in this case the tangential pressure dominates, generating an outward (repulsive) force that helps sustain the throat. When $\Delta(r) = 0$, the pressures are isotropic, with radial and tangential components equal [118–120]. Anisotropic pressure plays a vital role in $\mathcal{WH}$ stability. Outward anisotropy ($\Delta > 0$) counterbalances gravity, preventing throat collapse and ensuring traversability. Studies [92,102,121] indicate that stable $\mathcal{WH}$ solutions can be achieved with suitable parameter choices governing the matter content. In the present work, with the three toy shape function models considered, the anisotropy parameter supports stable behavior for suitable parameter ranges. Anisotropy in WH models may arise due to:

- $\mathcal{EM}$: Matter that violates energy conditions often induces anisotropic stresses that affect the WH geometry.
- $\mathcal{GMC}$ fields: The $\mathcal{GMC}$ (α) modifies the pressure anisotropy, influencing the structure and stability.
- $\mathcal{AGT}$ corrections: $f(R)$ gravity corrections, parameterized by β, introduce anisotropic geometric contributions beyond $\mathcal{GTR}$.

5.3.1 *Anisotropy parameter expressions for the three models*

We now explicitly give the anisotropy parameters $\Delta(r)$ for the three shape function models analyzed in this work. For the first model, the anisotropy parameter reads

$$\begin{aligned}\Delta = \frac{1}{2r^8}\Big[& -4\tau_1\alpha^2 a_0^2 r^2\big(r^2 - 6\beta\big(5\alpha^2+3\big)\big) \\ & -2\big(\alpha^2-1\big)r^4\big(4\big(7\beta\alpha^2+\beta\big)+r^2\big) \\ & +3(\tau_1+1)\alpha^2 a_0 r^3\big(20\beta\big(\alpha^2-1\big)+r^2\big) \\ & +208\tau_1^2\beta\alpha^4 a_0^4 - 196\tau_1(\tau_1+1)\beta\alpha^4 a_0^3 r\Big] \end{aligned} \tag{48}$$

Figure 19(a) shows the variation of Δ with respect to r for model 1 with various α and β, and a fixed throat radius $a_0 = 1$:

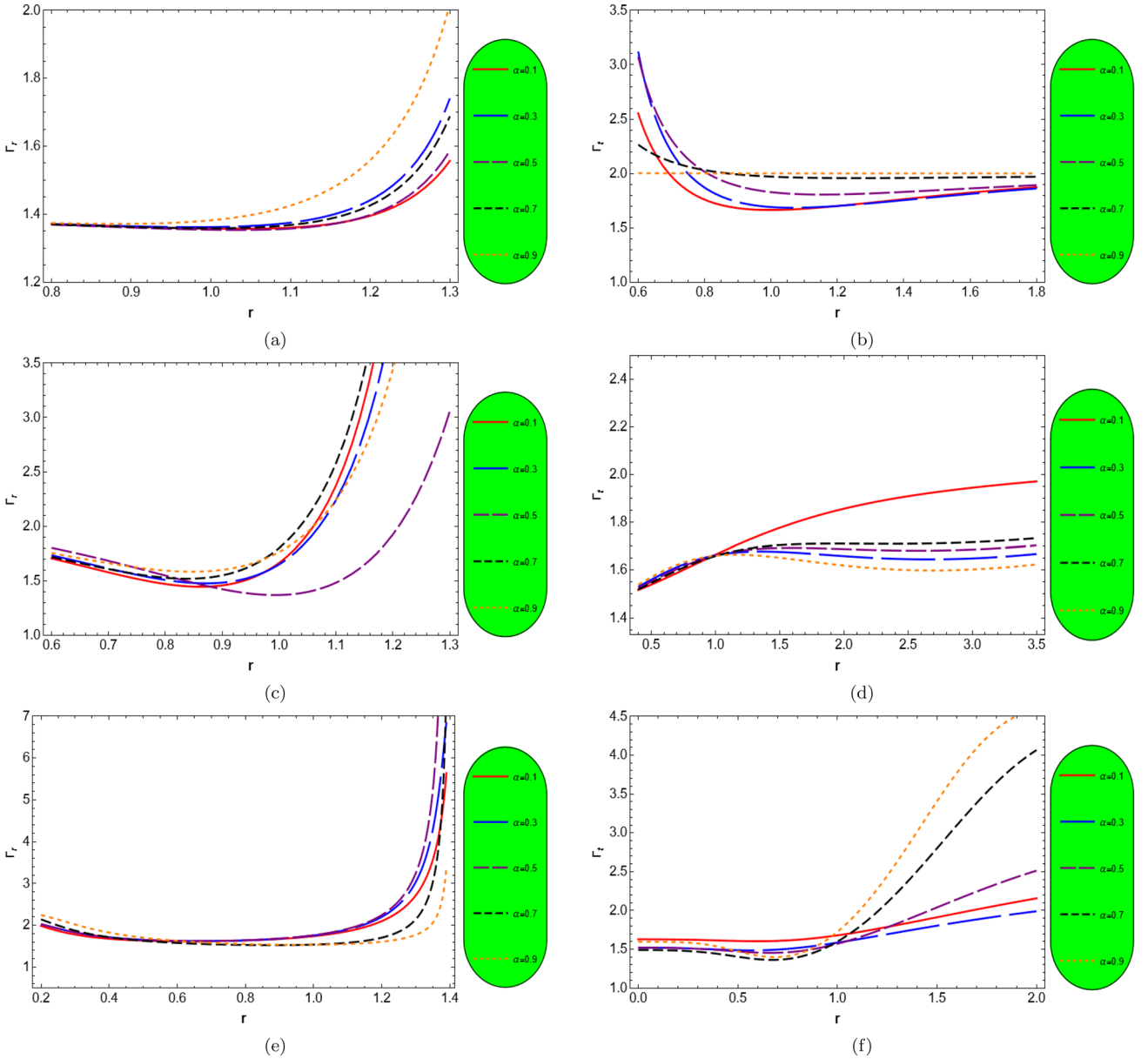

Fig. 18 Profile of adiabatic index corresponding to model-1 in panels (**a**), (**b**), for model-2 in panels (**c**), (**d**), and model-3 in panels (**e**), (**f**) respectively, as function of r for different values of $\mathcal{GMC}$ $0 < \alpha < 1$, throat radius $a_0 = 1$ and different values of correction parameter β along with some values of model parameters τ_1, τ_2, and τ_3

The anisotropy remains positive throughout the domain, indicating that anisotropic pressures induce a repulsive force that can counterbalance gravitational collapse and sustain an open $\mathcal{WH}$ throat. The anisotropy parameter for the second model (exponential form) is given by

$$\Delta = \frac{1}{2r^4}\Big(\tau_2\alpha^2 r^3 e^{\tau_2(a_0-r)}\big(4\tau_2^2\beta\alpha^2\big(3e^{\tau_2(a_0-r)}-2\big)+1\big) + 2r^2\big(2\tau_2^2\beta\alpha^4 e^{\tau_2(a_0-r)}\big(3e^{\tau_2(a_0-r)}-4\big)+\alpha^2\big(e^{\tau_2(a_0-r)} - 1\big)+1\big) - 4\tau_2\beta\alpha^2 r e^{\tau_2(a_0-r)}\big(7\alpha^2\big(e^{\tau_2(a_0-r)}-1\big)+3\big) - 8\beta\big(7\alpha^4\big(e^{\tau_2(a_0-r)}-1\big)^2+6\alpha^2\big(e^{\tau_2(a_0-r)}-1\big)-1\big)\Big) \quad (49)$$

The corresponding graphical illustration of model 2 is shown in Fig. 19(b):

[H] Here, Δ remains positive over the domain considered, signifying repulsive anisotropic forces that help prevent gravitational collapse and maintain the $\mathcal{WH}$ throat open. For the third model (arctangent shape function), the anisotropy parameter is expressed as

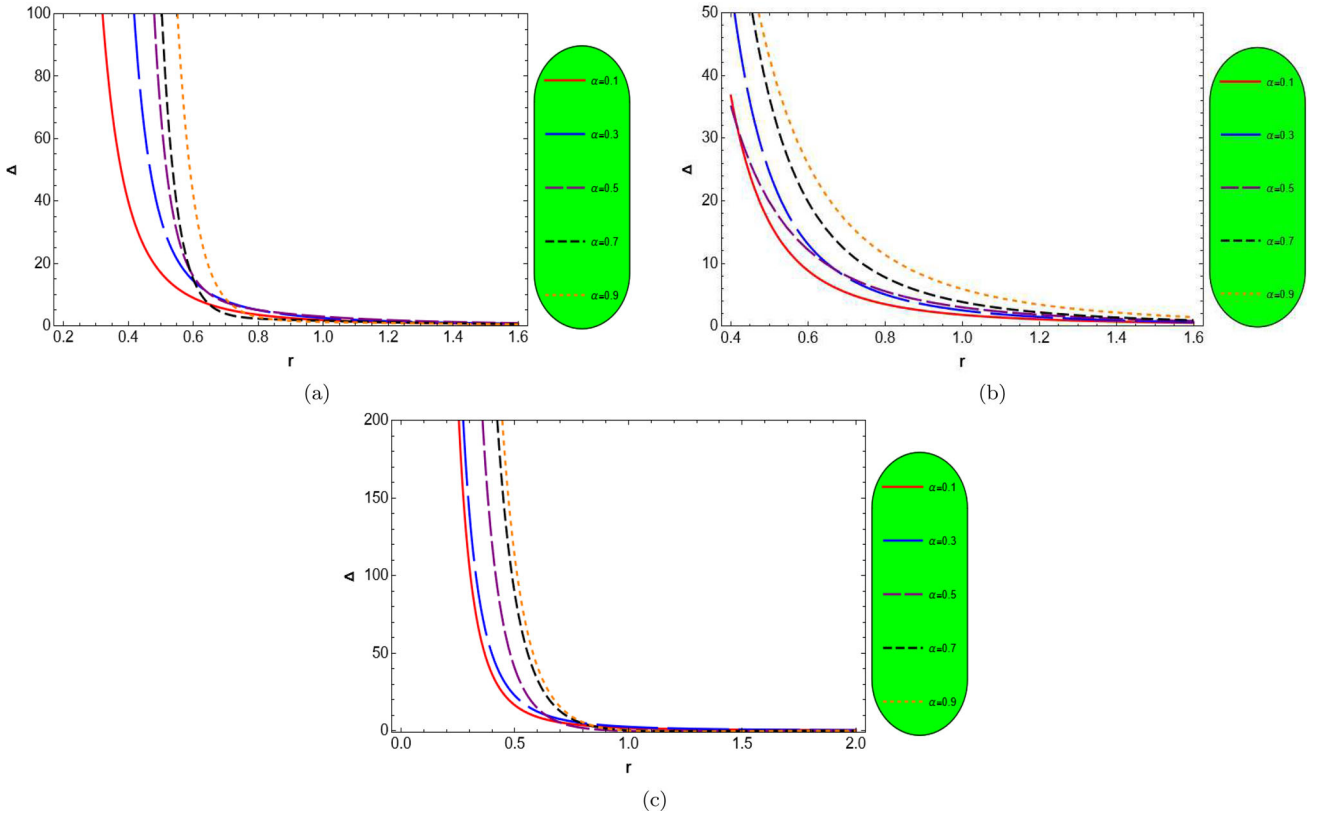

Fig. 19 Profile of the anisotropy parameter for model-1 Δ as a function of the radial coordinate r for varying $\mathcal{GMC}$ $0 < \alpha < 1$, fixed throat radius $a_0 = 1$, and different correction parameters and shape function model parameters

$$\begin{aligned}\Delta = \frac{1}{2r^5\left(\tau_3^2 r^2+1\right)^3}\Big(& -4a_0^2\tau_3\beta\alpha^4\big(\big(49\tau_3^4 r^4 \\ & +48\tau_3^2 r^2+15\big)\tan^{-1}(\tau_3 r)-\tau_3 r\left(3\tau_3^2 r^2+1\right)\big) \\ & +a_0\alpha^2\left(3\left(\tau_3^2 r^2+1\right)^3\right. \\ & \times\tan^{-1}(\tau_3 r)\left(20\beta\left(\alpha^2-1\right)+r^2\right) \\ & +\tau_3 r\big(-\tau_3^4 r^6+2\tau_3^2 r^4\left(6\tau_3^2\left(15\beta\alpha^2+\beta\right)-1\right) \\ & +r^2\left(24\tau_3^2\left(7\beta\alpha^2+\beta\right)-1\right) \\ & \left.+4\beta\left(13\alpha^2+3\right)\big)\right) \\ & -2\left(\alpha^2-1\right)r\left(\tau_3^2 r^2+1\right)^3\left(4\left(7\beta\alpha^2+\beta\right)+r^2\right)\Big) \end{aligned} \quad (50)$$

The behavior of Δ is depicted in Fig. 19(c):

As visible in Fig. 19(c), $\Delta > 0$ in the examined radial domain, indicating the dominance of repulsive anisotropic forces that stabilize the throat of the $\mathcal{WH}$ and prevent collapse. In the background of our considered $\mathcal{AGT}$ model with $\mathcal{GMC}$ the graphical and analytical results of all three models consistently show that the anisotropy parameter $\Delta(r)$ remains positive over relevant parameter regions. This emphasize its role in generating repulsive pressure components that can counterbalance the inward gravitational forces near the $\mathcal{WH}$ throat.

5.4 Analysis of exotic matter via VIQ in the three wormhole models

In $\mathcal{GTR}$, for physical viability the amount of $\mathcal{EM}$ should be minimal while concept of VIQ introduced to systematically evaluate the total amount of $\mathcal{EM}$ in a given $\mathcal{WH}$ configuration. This tool quantifies the integrated violation of the $\mathcal{NEC}$ throughout the spatial volume of the $\mathcal{WH}$. Mathematically:

$$VIQ = \oint \left(\rho(r) + p_r(r)\right) dV, \quad (51)$$

here $dV = r^2 dr\, d\Omega$ and $d\Omega$ represents the solid angle.

The VIQ evaluates the cumulative effect of $\mathcal{NEC}$ violation throughout the $\mathcal{WH}$ geometry, while a large negative value indicates significant $\mathcal{EM}$. A small or nearly zero value suggests a physically viable $\mathcal{WH}$ requiring minimal electromagnetic stimulation. The VIQ used in our computations:

$$VIQ = 8\pi \int_{a_0}^{R_1} \left(\rho(r) + p_r(r)\right) r^2 dr, \quad (52)$$

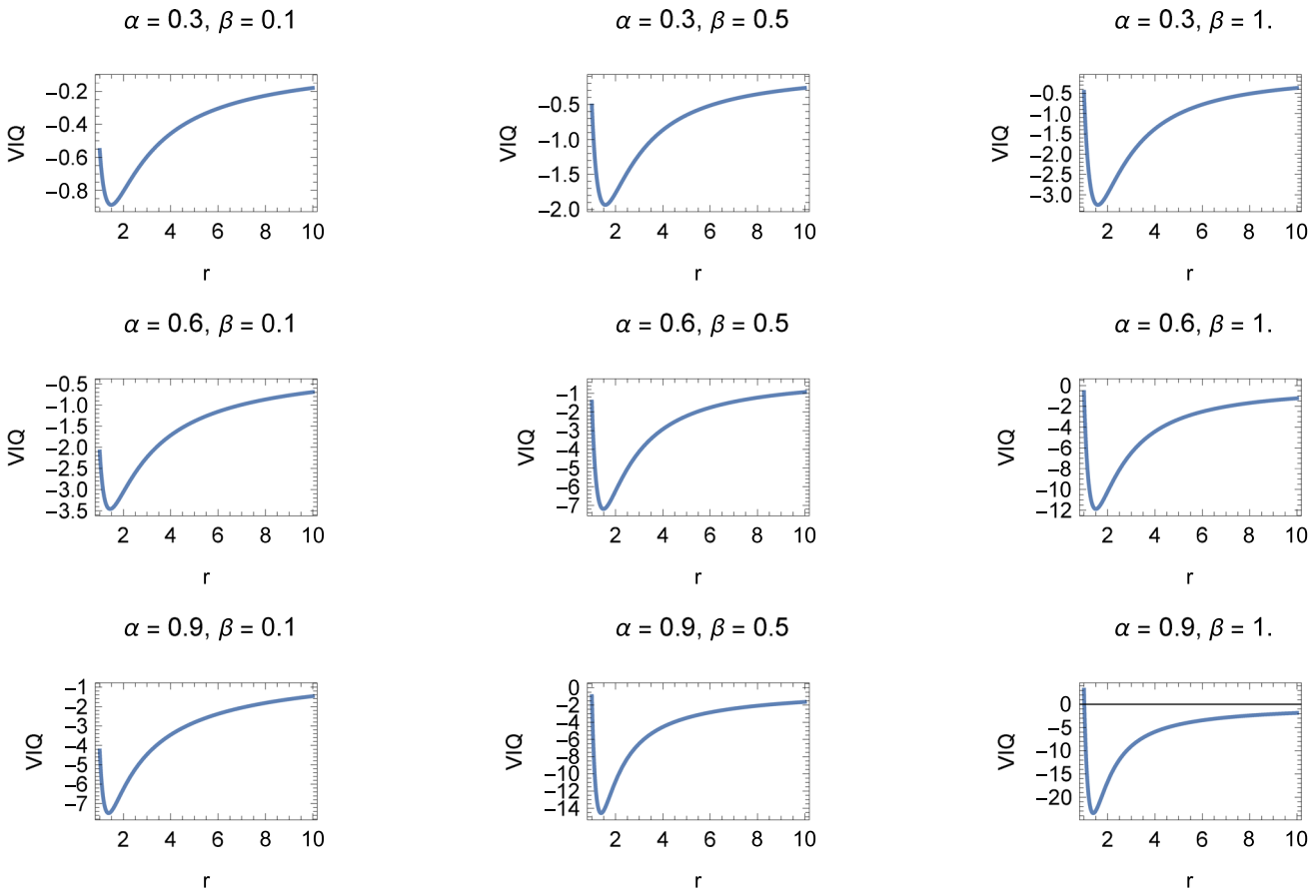

Fig. 20 Graphs of VIQ for model-1 with fixed $\beta = 0.5$, $a_0 = 1$, $\tau_1 = 0.5$, and varying $\alpha = 0.3, 0.6, 0.9$

here R_1 is a finite upper limit of integration. To visualize and contrast these features across models, we analyze the integrand incorporating the spherical volume element to reflect the local contribution of $\mathcal{EM}$ at radius r. Figures 20, 21 and 22 display these integrands as functions of r for each model, systematically varying $\mathcal{GMC}$ α and β, while fixing a_0 and respective shape function parameters. Key observations across models in the background of our considered $\mathcal{AGT}$ model with $\mathcal{GMC}$:

- In all three models, the $\mathcal{NEC}$ violation indicated by negative values of VIQ is primarily localized near the $\mathcal{WH}$ throat ($r = a_0$), with the integrand approaching zero or positive values at larger radial distances.
- The localization of $\mathcal{EM}$ is physically favorable, suggesting that the $\mathcal{EM}$ required to keep the throat open does not pervade the entire spacetime, thereby alleviating concerns regarding global exoticity under the influence of $\mathcal{AGT}$ model with $\mathcal{GMC}$ parameter.
- Increasing α tends to enhance both the magnitude and spatial extent of $\mathcal{NEC}$ violation in each model. For smaller α values, the $\mathcal{EM}$ content is significantly reduced, implying potential parameter regimes where exoticity is minimized.
- $\mathcal{AGT}$ correction parameter β, as larger values of this correction factor generally increase the degree of $\mathcal{NEC}$ violation across all models in $f(R)$ gravity thus contribute to greater demands for $\mathcal{EM}$.
- Shape function model one exhibits a relatively sharp $\mathcal{NEC}$ violation localized very close to the throat, with pronounced sensitivity to both parameters
- Second shape function model shows a somewhat broader $\mathcal{EM}$ region with a smoother transition towards the asymptotic radius, providing slightly less steep gradients in VIQ.
- While third shape function model features the most gradual tail-off of the $\mathcal{EM}$ integrand, reflecting the more intricate radial dependence.

These figures underscores the importance of parameter tuning to optimize $\mathcal{WH}$ viability and the presence of a $\mathcal{GMC}$ significantly influences the $\mathcal{EM}$ distribution, highlighting the interplay between topological defects and gravitational configurations in $\mathcal{AGT}$s.

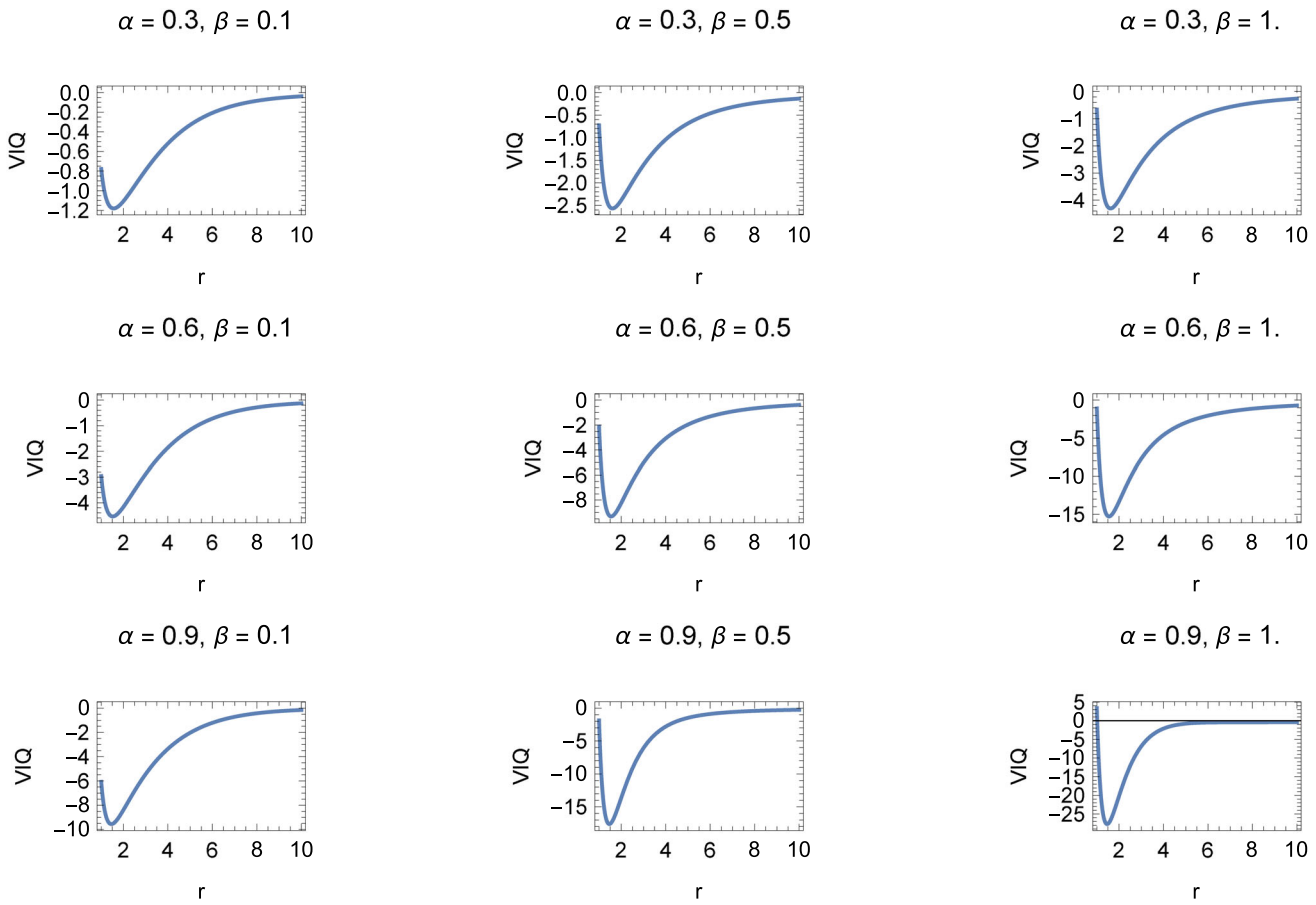

Fig. 21 Graphs of VIQ for model-2 with fixed $\alpha = 0.6$, $a_0 = 1$, $\tau_2 = 0.5$, and varying $\beta = 0.1, 0.5, 1.0$

6 Concluding remarks

We explored the geometrical and physical characteristics of static, spherically symmetric Morris–Thorne like $\mathcal{WH}$ solutions with a $\mathcal{GMC}$ in the context of power-law gravity, i.e., $f(R)$ gravity, specifically employing the Starobinsky model. By investigating a range of shape functions and analyzing their influence via 2D and 3D embedding diagrams, we illuminated how the $\mathcal{GMC}$ modifies the $\mathcal{WH}$ geometry, throat size, and overall traversability, by adopting an anisotropic $\mathcal{EMT}$, we solved the modified field equations and conducted a thorough examination of the energy conditions, i.e., ($\mathcal{NEC}$s, $\mathcal{WEC}$s, $\mathcal{SEC}$s, $\mathcal{DEC}$s), while our findings indicate that, within this particular $f(R)$ gravity regime, the requirement for $\mathcal{EM}$ to sustain traversable $\mathcal{WH}$s can be significantly relaxed compared to $\mathcal{GTR}$. Furthermore, we find that the $\mathcal{GMC}$, characterized by the parameter α, significantly affects the energy conditions. The presence of higher-order curvature terms from the modified $f(R)$ theory also contributes to the geometry of the $\mathcal{WH}$, as these terms arise from the effective stress energy tensor.

In many cases, the effective $\mathcal{EMT}$ arising from the geometric modifications allow for the fulfillment of classical energy conditions, suggesting that non-exotic, physically reasonable matter may suffice to support the $\mathcal{WH}$ structure in the background of our considered $\mathcal{AGT}$ model with $\mathcal{GMC}$. We also performed a detailed stability analysis using several physical and geometrical criteria: (i) causality approach, (ii) Herrera's cracking concept/technique, and (iii) adiabatic index method. We investigated the behavior of the anisotropy parameter, i.e., anisotropic effects which showed the impact on the stability of constructed $\mathcal{WHH}$ models with $\mathcal{GMC}$. Furthermore, the anisotropy parameter for each model, showing that both the $\mathcal{GMC}$ α and the relativistic correction parameter β govern the repulsive behavior of the $\mathcal{WH}$ geometry in our case study, ultimately confirming its stability.

Our findings show that the $\mathcal{GMC}$ can enhance the stability of these configurations by yielding larger throat radii and flatter embeddings. These properties are potentially beneficial for traversability and physical viability. The evaluation of the VIQ further quantifies the total amount of $\mathcal{EM}$ potentially required, with results indicating minimized exoticity for certain shape functions and parameter choices.

These results not only increase our understanding of $\mathcal{WH}$ physics in some extended theories of gravity that goes beyond the $\mathcal{GTR}$, but also highlight the significant role of $f(R)$ $\mathcal{AGT}$

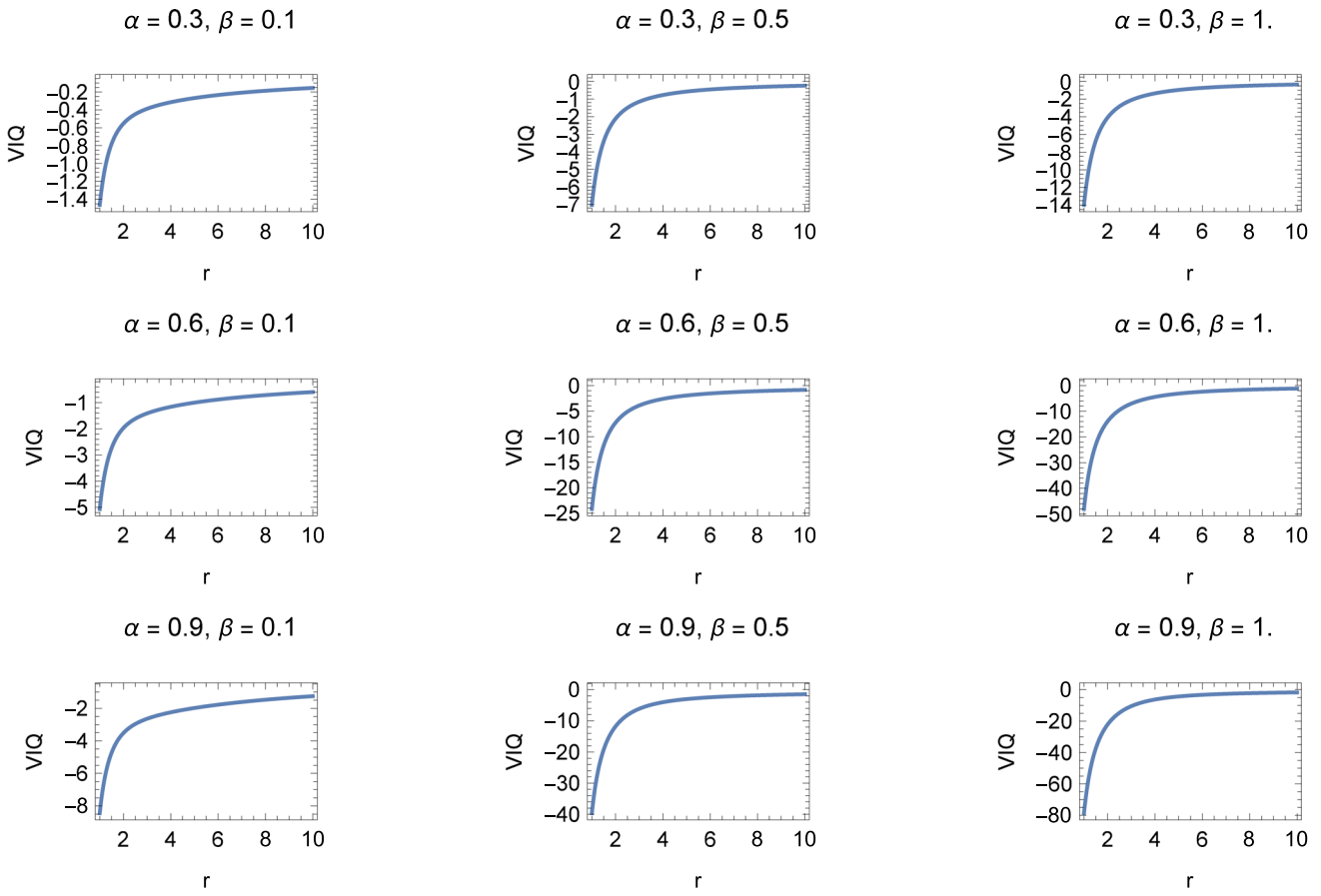

Fig. 22 Graphs of VIQ for model-3 with fixed $\alpha = 0.6$, $a_0 = 1$, $\tau_3 = 0.5$, and varying $\beta = 0.1, 0.5, 1.0$

model in the search for physically plausible traversable $\mathcal{WH}$ solutions without resorting to unphysical matter content. Furthermore, this study improves our understanding of the potential for the physical realization of Morris–Thorne like $\mathcal{WH}$s with a $\mathcal{GMC}$ by exploring the impact of different shape functions on the energy conditions with power-law gravity.

Acknowledgements The authors extend their appreciation to the Deanship of Research and Graduate Studies at King Khalid University for funding this work through a Large Research Project under grant number RGP2/407/46. The author SKM is thankful to the UoN administration for continuous support and encouragement for the research work.

Data Availability Statement This manuscript has no associated data. [Authors' comment: Data sharing not applicable to this article as no datasets were generated or analyzed during the current study.]

Code Availability Statement This manuscript has no associated code/software. [Authors' comment: Code/Software sharing not applicable to this article as no code/software was generated or analysed during the current study. The current work has already included a comprehensive analysis and the corresponding calculations.]

Funded by SCOAP[3].

References

1. A.G. Riess et al., Astron. J. **116**, 1009 (1998)
2. S. Perlmutter, G. Aldering, G. Goldhaber, R.A. Knop, P. Nugent, P.G. Castro, S. Deustua, S. Fabbro, A. Goobar, D.E. Groom, Astrophys. J. **517**, 565 (1999)
3. A.G. Riess et al., Astrophys. J. **659**, 98 (2007)
4. D. Rabounski, Prog. Phys. **2**, 6 (2012)
5. P.J.E. Peebles, Rev. Mod. Phys. **75**, 559 (2003)
6. S. Nojiri, S.D. Odintsov, Phys. Lett. B **639**, 144 (2006)
7. T. CliftonFerreira et al., Phys. Rep. **513**, 1 (2012)
8. S. Nojiri, S. Odintsov, Phys. Rep. **692**, 1 (2017)
9. E.E. Flanagan, Class. Quantum Gravity **21**(2), 417 (2003)
10. J.D. Bekenstein, Phys. Rev. D **70**(8), 083509 (2004)

11. K. Becker, M. Becker, J.H. Schwarz, *String theory and M-theory: A modern introduction* (2006)
12. J. Santos, J. Alcaniz, M. Reboucas, F. Carvalho, Phys. Rev. D-Part. Fields Gravit. Cosmol. **76**(8), 083513 (2007)
13. P.D. Mannheim, Found. Phys. **42**, 388 (2012)
14. J. Rayimbaev, P. Tadjimuratov, Phys. Rev. D **102**, 024019 (2020)
15. Z. Yousaf, Phys. Dark Univ. **48**, 101884 (2025)
16. H.A. Buchdahl, Mon. Not. R. Astron. Soc. **150**(1), 1 (1970)
17. A.A. Starobinsky, Phys. Lett. B **91**(1), 99 (1980)
18. S. Nojiri, S.D. Odintsov, Phys. Rev. D **68**(12), 123512 (2003)
19. S. Nojiri, S.D. Odintsov, Int. J. Geom. Methods Mod. Phys. **4**(01), 115 (2007)
20. W. Hu, I. Sawicki, Phys. Rev. D-Part. Fields Gravit. Cosmol. **76**(6), 064004 (2007)
21. M. Martinelli, Nucl. Phys. B (Proceedings Supplements) **194**, 266 (2009)
22. A.V. Astashenok, S. Capozziello, S.D. Odintsov, J. Cosmol. Astropart. Phys. **2013**, 040 (2013)
23. A.V. Astashenok, S. Capozziello, S.D. Odintsov, J. Cosmol. Astropart. Phys. **2015**, 001 (2015)
24. M. Yousaf, H. Asad, A. Rehman, Phys. Dark Univ. **48**, 101888 (2025)
25. M.Z. Gul, M. Sharif, A. Arooj, Fortschr. der Phys. **72**, 2300221 (2024)
26. K. Bamba, Y. Kokusho, S. Nojiri, N. Shirai, Class. Quantum Gravity **31**, 075016 (2014)
27. S. Capozziello, M. De Laurentis, Phys. Rep. **509**, 167 (2011)
28. A.V. Astashenok, K. Mosani, S.D. Odintsov et al., Int. J. Geom. Methods Mod. Phys. **16**, 1950035 (2019)
29. L. Flamm, Beiträge zur Einsteinschen gravitationstheorie. Hirzel (1916)
30. A. Einstein, N. Rosen, Phys. Rev. **48**(1), 73 (1935)
31. R.W. Fuller, J.A. Wheeler, Phys. Rev. **128**(2), 919 (1962)
32. H.G. Ellis, J. Math. Phys. **14**(1), 104 (1973)
33. K. Bronnikov, Acta. Phys. Pol. B4 (1973)
34. M.S. Morris, Am. J. Phys. **56**(5), 395 (1988)
35. A. Wang, P.S. Letelier, Prog. Theor. Phys. **94**(1), 137 (1995)
36. M. Visser, Phys. Rev. D **54**(8), 5103 (1996)
37. M. Visser, D. Hochberg, Ann Israel Phys. Soc. **13**, 249 (1997)
38. D. Hochberg, M. Visser, Phys. Rev. Lett. **81**(4), 746 (1998)
39. D. Hochberg, M. Visser, Phys. Rev. D **58**(4), 044021 (1998)
40. F.S. Lobo, M.A. Oliveira, Phys. Rev. D-Part. Fields Gravit. Cosmol. **80**(10), 104012 (2009)
41. N. Godani, G.C. Samanta, Chin. J. Phys. **62**, 161 (2019)
42. M. Yousaf, H. Asad, Phys. Dark Univ. **48**, 101841 (2025)
43. A. Rehman, T. Naseer, N. Alessa, A.-H. Abdel-Aty, Nucl. Phys. B **1015**, 116897 (2025)
44. K. Bronnikov, S.-W. Kim, Phys. Rev. D **67**(6), 064027 (2003)
45. N. Furey, A. De Benedictis, Class. Quantum Gravity **22**(2), 313 (2004)
46. S. Biswas, C. Singha, S. Chakraborty, Phys. Rev. D **109**, 064043 (2024)
47. Y. Yang, D. Liu, A. Övgün, G. Lambiase, Z.-W. Long, Eur. Phys. J. C **84**, 63 (2024)
48. M.V.D.S. Silva, G. Alencar, R.C. Filho, R. Neves, C.R. Muniz, Eur. Phys. J. Plus **140**, 289 (2025)
49. A. Waseem, F. Javed, M.Z. Gul, G. Mustafa, A. Errehymy, Eur. Phys. J. C **83**, 1088 (2023)
50. A. Ditta, I. Hussain, G. Mustafa, A. Errehymy, M. Daoud, Eur. Phys. J. C **81**, 880 (2021)
51. F. Abdulxamidov, C.A. Benavides-Gallego, W.-B. Han, J. Rayimbaev, A. Abdujabbarov, Phys. Rev. D **106**, 024012 (2022)
52. B. Toshmatov, K. Mavlyanov, B. Abdulazizov, A. Mamadjanov, Ann. Phys. **458**, 169450 (2023)
53. P. Channuie, A. Ditta, N. Kaewkhao, Phys. Dark Univ. **50**, 101963 (2025)
54. M.Z. Gul, F. Ni, M. Sharif, S. Zahid, Phys. Dark Univ. **49**, 101981 (2025)
55. M.Z. Gul, M. Sharif, Eur. Phys. J. C **84**, 802 (2024)
56. M.Z. Gul, M. Sharif, Phys. Dark Univ. **45**, 101537 (2024)
57. N. Fatima, M.Z. Gul, M. Sharif, S. Shabbir, Nucl. Phys. B **1016**, 116923 (2025)
58. M.M.M. Nasir, M.Z. Gul, O. Donmez, F. Javed, B. Almutairi, Eur. Phys. J. C **85**, 189 (2025)
59. S. Rani, M. Adeel, M.Z. Gul, A. Jawad, S. Shaymatov, Phys. Dark Univ. **47**, 101754 (2025)
60. I. Hashim, M. Sharif, M.Z. Gul, High Energy Density Phys. **57**, 101223 (2025)
61. G. Nan, M.Z. Gul, M. Sharif, A. Arooj, Phys. Dark Univ. **46**, 101635 (2024)
62. T. Naseer, A. Rehman, M. Sharif, N. Alessa, A.-H. Abdel-Aty, Phys. Dark Univ. **48**, 101958 (2025)
63. A. Rehman, T. Naseer, B. Dayanandan, Nucl. Phys. B **1013**, 116852 (2025)
64. T. Naseer, Eur. Phys. J. C **84**(12), 1256 (2024)
65. C. Qiao, X. Long, L. Yang, Y. Zhu, W. Cai, Astrophys. J. **991**, 46 (2025)
66. G. Feng, S. Yu, T. Wang, Z. Zhang, Ann. Phys. **473**, 169903 (2025)
67. T. Naseer, M. Sharif, Phys. Scr. **99**, 095028 (2024)
68. P. Pavlovic, M. Sossich, Euro. Phys. J. C **75**, 1 (2015)
69. H. Golchin, M.R. Mehdizadeh, Eur. Phys. J. C **79**, 1 (2019)
70. N. Godani, Int. J. Geom. Methods Mod. Phys. **19**, 2250035 (2022)
71. M. Yousaf, M.Z. Bhatti, Z. Yousaf, Nucl. Phys. B **995**, 116328 (2023)
72. M.Z. Bhatti, Z. Yousaf, M. Yousaf, Gen. Relativ. Gravit. **56**, 3 (2024)
73. R. Konoplya, A. Zhidenko, J. Cosmol. Astropart. Phys. **14**, 043 (2016)
74. F. Rahaman, M. Kalam, K.A. Rahman, Mod. Phys. Lett. A **23**, 1199 (2008)
75. F.S. Lobo, Class. Quantum Gravity **25**(17), 175006 (2008)
76. M.Z. Bhatti, Z. Yousaf, M. Yousaf, Commun. Theor. Phys. **75**, 125401 (2023)
77. G. Murtaza, A. Ditta, T. Naseer et al., J. High Energy Astrophys. **44**, 279 (2024)
78. T. Naseer, M. Sharif, M. Faiza et al., Eur. Phys. J. C **84**, 1187 (2024)
79. M. Yousaf, H. Asad, M. Aslam, High Energy Density Phys. **57**, 101221 (2025)
80. G.C. Samanta, N. Godani, K. Bamba, Int. J. Mod. Phys. D **29**(09), 2050068 (2020)
81. Z. Yousaf, M. Rizwan, M. Alshammari, O.A. Almatroud, S. Alshammari, M.M. Al-sawalha, Eur. Phys. J. C **85**, 998 (2025)
82. I. Hussain, G. Mustafa, K.A. Yasir, A. Ditta, Chin. J. Phys. **77**, 1253–1268 (2022)
83. A. Saleem, Z. Ali, A. Bouzenada, A. Ditta, F. Atamurotov, G. Mustafa, Nucl. Phys. B **1018**, 117008 (2025)
84. A. Ditta, S. Sadiq, A. Rasheed, A. Errehymy, S.K. Maurya, G. Mustafa, Int. J. Geom. Methods Mod. Phys. **0**, 2550182 (2025)
85. T. Naseer, M. Sharif, M. Faiza, W. Albalawi, A.-H. Abdel-Aty, Phys. Dark Univ. **48**, 101890 (2025)
86. M.Z. Bhatti, M. Yousaf, Z. Yousaf, Gen. Relativ. Gravit. **55**, 16 (2023)
87. U. Farwa, A. Abbas, M. Yousaf, Nucl. Phys. B **1018**, 117086 (2025)
88. M. Yousaf, H. Asad, B. Almutairi, S. Hasan, A.S. Khan, Phys. Scr. **99**, 115270 (2024)
89. T. Naseer, Astropart. Phys. **166**, 103073 (2025)
90. H. Asad, M. Yousaf, B. Almutairi, L. Zahid, A.S. Khan, Phys. Dark Univ. **46**, 101666 (2024)
91. J. Goswami, H. Rahman, R. Sikdar, R. Parvin, F. Ahmed, Eur. Phys. J. C **84**, 1037 (2024)

92. E. Dai, M. Yousaf, F. Javed et al., Nucl. Phys. B **1018**, 117017 (2025)
93. A. Vilenkin, A. Vilenkin, E. Shellard, *Cosmic Strings and Other Topological Defects* (Cambridge University Press, Cambridge, 1994)
94. T.W. Kibble, J. Phys. A Math. Gen. **9**, 1387 (1976)
95. S. Sarkar, N. Sarkar, F. Rahaman, Eur. Phys. J. C **80**, 882 (2020)
96. M. Barriola, A. Vilenkin, Phys. Rev. Lett. **63**, 341 (1989)
97. E.R. Bezerra de Mello, Braz. J. Phys. **31**, 211 (2001)
98. F. Ahmed, J. Cosmol. Astropart. Phys. **2023**, 082 (2023)
99. F. Ahmed, Acta Phys. Polon. B **55**, 1 (2024)
100. D.J. Gogoi, U.D. Goswami, J. Cosmol. Astropart. Phys. **2023**, 027 (2023)
101. T. Naseer, M. Sharif, Phys. Dark Univ. **46**, 101595 (2024)
102. F. Rahaman, S. Sarkar, K.N. Singh, N. Pant, Mod. Phys. Lett. A **34**, 1950010 (2019)
103. L. Tsui, P. Leung, Astrophys. J. **631**, 495 (2005)
104. O. Benhar, V. Ferrari, L. Gualtieri, S. Marassi, Phys. Rev. D **72**, 044028 (2005)
105. S.-C. Leung, M.-C. Chu, L.-M. Lin, Phys. Rev. D **84**, 107301 (2011)
106. S.H. Voelkel, K.D. Kokkotas, Class. Quantum Gravity **34**, 175015 (2017)
107. M.Z. Bhatti, Z. Yousaf, M. Yousaf, Int. J. Geom. Methods. Mod. Phys. **19**, 2250120 (2022)
108. M. Yousaf, B. Almutairi, M.Z. Bhatti, Z. Yousaf, A.S. Khan, Commun. Theor. Phys. **77**, 035403 (2024)
109. B. Almutairi, M.Z. Bhatti, M. Yousaf et al., Int. J. Theor. Phys. **63**, 215 (2024)
110. P. Luz, S. Carloni, Phys. Rev. D **110**, 084055 (2024)
111. M. Yousaf, Chin. J. Phys. **95**, 1278–1302 (2025)
112. H. Abreu, H. Hernández, L.A. Núnez, Class. Quantum Gravity **24**, 4631 (2007)
113. T. Naseer, M. Sharif, F. Chand, Phys. Dark Univ. **47**, 101783 (2025)
114. L. Herrera, Phys. Lett. A, **165**(3), 206–210 (1992)
115. M. Yousaf, H. Asad, A. Rehman, M. Shahzad, J. Rayimbaev, E. Davletov, Phys. Dark Univ. **50**, 102123 (2025)
116. H. Heintzmann, W. Hillebrandt, Astron. Astrophys. **38**, 51 (1975)
117. M. Bhatti, Z. Yousaf, M. Yousaf, Int. J. Geom. Methods Mod. Phys. **19**, 2250018 (2022)
118. M. Yousaf, B.S. Alkahtani, G. Mustafa, S.K. Maurya, Chin. J. Phys. **97**, 1255 (2025)
119. M. Yousaf, I. Shahid, O. Rahimov, A.S. Alqahtani, Int. J. Geom. Methods Mod. Phys. (2025). https://doi.org/10.1142/S021988782650060X
120. M.Z. Bhatti, A. Adeel, M. Yousaf, Int. J. Geom. Methods Mod. Phys. (2025). https://doi.org/10.1142/S0219887825502093
121. H. Asad, M. Yousaf, U. Zafar, J. Rayimbaev, A. Dauletov, Fortschr. der Phys. **73**, e70034 (2025)